Spliceosomal disruption of the non-canonical BAF complex in cancer

Daichi Inoue[1,2,*], **Guo-Liang Chew**[3,*], **Bo Liu**[1], **Brittany C. Michel**[4,5,6], **Joseph Pangallo**[3], **Andrew R. D'Avino**[5,6], **Tyler Hitchman**[1], **Khrystyna North**[3,7], **Stanley Chun-Wei Lee**[1], **Lillian Bitner**[1], **Ariele Block**[1], **Amanda R. Moore**[1], **Akihide Yoshimi**[1], **Luisa Escobar-Hoyos**[1], **Hana Cho**[1], **Alex Penson**[1], **Sydney X. Lu**[1], **Justin Taylor**[1], **Yu Chen**[1,8], **Cigall Kadoch**[5,6], **Omar Abdel-Wahab**[1,8,**], **Robert K. Bradley**[3,7,**]

[1]Human Oncology and Pathogenesis Program, Memorial Sloan Kettering Cancer Center, New York, NY 10065, USA

[2]Department of Hematology-Oncology, Institute of Biomedical Research and Innovation, Foundation for Biomedical Research and Innovation at Kobe, Kobe, Hyogo 6500047, Japan

[3]Computational Biology Program, Public Health Sciences Division, Fred Hutchinson Cancer Research Center, Seattle, WA 98109, USA; Basic Sciences Division, Fred Hutchinson Cancer Research Center, Seattle, WA 98109, USA

[4]Department of Pediatric Oncology, Dana-Farber Cancer Institute and Harvard Medical School, Boston, MA, USA

[5]Broad Institute of MIT and Harvard, Cambridge, MA, USA

[6]Biomedical and Biological Sciences Program, Harvard Medical School, Boston, MA, USA

[7]Department of Genome Sciences, University of Washington, Seattle, WA 98195, USA

[8]Department of Medicine, Memorial Sloan Kettering Cancer Center, New York, NY 10065, USA

Abstract

SF3B1 is the most commonly mutated RNA splicing factor in cancer[1–4], but the mechanisms by which *SF3B1* mutations promote malignancy are poorly understood. Here, we integrated pan-

cancer splicing analyses with a positive enrichment CRISPR screen to prioritize splicing alterations that promote tumorigenesis. We report that diverse *SF3B1* mutations converge on repression of BRD9, a core component of the recently described GLTSCR1/1L-containing non-canonical BAF (ncBAF) chromatin remodeling complex[5–7]. Mutant SF3B1 recognizes an aberrant deep intronic branchpoint within *BRD9*, thereby inducing inclusion of an endogenous retroviral element-derived poison exon and BRD9 mRNA degradation. BRD9 depletion causes loss of ncBAF at CTCF-associated loci and promotes melanomagenesis. BRD9 is a potent tumor suppressor in uveal melanoma (UVM), such that correcting *BRD9* mis-splicing in *SF3B1*-mutant cells with antisense oligonucleotides (ASOs) or CRISPR-directed mutagenesis suppresses tumor growth. Our results implicate ncBAF disruption in the diverse cancers carrying *SF3B1* mutations and suggest a mechanism-based therapeutic for these malignancies.

SF3B1 is subject to recurrent missense mutations at specific residues in myeloid[1,2] and lymphoid[3,8] leukemias as well as solid tumors, at rates of up to 14-29% (UVM[9–12]) and 65-83% (myelodysplastic syndromes with ring sideroblasts[1,2]). Consistent with SF3B1's critical role in 3' splice site (3'ss) recognition[13], several studies reported that *SF3B1* mutations induce widespread usage of abnormal 3'ss[10,14,15]. Although many mis-spliced genes have been identified in *SF3B1*-mutant samples, few have been functionally implicated in driving disease.

We hypothesized that effectors of *SF3B1* mutations' pro-tumorigenic effects might appear as pan-cancer targets of mutant SF3B1. We accordingly identified mis-spliced events shared between erythroleukemic (K562) and UVM (MEL270) cells expressing wild-type (WT) *SF3B1* or the most common *SF3B1* mutation (*SF3B1*K700E). A compact set of 40 events exhibited concordant splicing changes and was sufficient to infer *SF3B1* mutational status across 249 chronic lymphocytic leukemia (CLL), MDS, and UVM samples (Fig. 1a, Extended Data Fig. 1a, Supplementary Tables 1–3).

We designed a single guide RNA (sgRNA) library targeting both pan-cancer and cancer type-specific targets of mutant SF3B1, focusing on genes for which *SF3B1* mutations are predicted to cause mis-splicing that triggers nonsense-mediated RNA decay (NMD; Fig. 1b, Supplementary Table 4). We tested whether knockout of any such gene promoted transformation of Ba/F3 cells (a spliceosome-WT cell line whose requirement for IL-3 can be overcome by oncogenic lesions; Fig. 1c). In addition to the positive control *Pten*, our screen revealed that *Brd9* loss promoted Ba/F3 transformation (Fig. 1d, Extended Data Fig. 1b–d, Supplementary Tables 5–6). *Brd9* was a notable hit because *BRD9* exhibited striking mis-splicing in all cancer cohorts (Fig. 1e). *Brd9* knockout conferred cytokine independence to 32Dcl3 cells and growth advantage to spliceosome-WT UVM, cutaneous melanoma, and pancreatic cancer cells (Extended Data Fig. 1d–f). In contrast, *MLL*-rearranged acute myeloid leukemia (AML) cells required BRD9 for growth (Extended Data Fig. 1g), as previously reported[16].

SF3B1 mutations cause exonization of a *BRD9* intronic sequence, resulting in inclusion of a poison exon that interrupts *BRD9*'s open reading frame. This *BRD9* poison exon is derived from a primate-specific endogenous retroviral element, explaining its absence from mice (Extended Data Fig. 1h–i). We confirmed that poison exon inclusion was induced by

expression of endogenous or ectopic mutant SF3B1 in K562 and NALM-6 cells, while *SF3B1* knockdown (KD) in *SF3B1*-WT cells had no effect (Extended Data Fig. 1j–m). The poison exon was included in an *SF3B1* mutation-dependent manner in diverse cell lines and CLL, MDS, and UVM samples bearing 19 different *SF3B1* mutations, but not healthy tissues (Extended Data Fig. 1m–p, Supplementary Table 7).

BRD9 poison exon inclusion triggered NMD and reduced BRD9 mRNA half-life and full-length BRD9 protein (Extended Data Fig. 1q–w). *SF3B1*-mutant patients exhibited reduced total BRD9 mRNA levels relative to WT patients (Extended Data Fig. 1x). We tested whether poison exon inclusion could result in production of C-terminally truncated BRD9 by knocking an N-terminal HA tag into the *BRD9* locus in MEL270 and K562 cells transgenically expressing WT or mutant SF3B1 (Extended Data Fig. 2a–c). Mutant SF3B1 suppressed full-length BRD9 levels without generating a truncated BRD9 protein (Fig. 1f).

SF3B1 mutations promote cryptic 3'ss usage[10,14,15], likely by altering SF3B1's normal role in branchpoint recognition[17]. We therefore mapped *BRD9* branchpoints used in K562, MEL270, and T47D (breast cancer) cells expressing mutant SF3B1 (Fig. 2a, Extended Data Fig. 2d–f). Poison exon inclusion was associated with an unusually close branchpoint (close branchpoints are rare and normally inefficiently recognized[18]). Mutating the aberrant branchpoint abolished poison exon recognition (Fig. 2b, Extended Data Fig. 2g). Consistent with the poison exon's lack of an obvious polypyrimidine tract, neither *U2AF1* nor *U2AF2* KD compromised poison exon recognition, while introducing a poly(Y) tract resulted in robust poison exon inclusion even in WT cells (Fig. 2b, Extended Data Fig. 2h–j). Finally, we identified a putative exonic splicing enhancer (ESE) that was essential for poison exon inclusion (Fig. 2c, Extended Data Fig. 2k). We confirmed the essentiality of the aberrant branchpoint, lack of a polypyrimidine tract, and ESE for poison exon recognition in the context of *SF3B1*R625H, the most common mutation in UVM (Extended Data Fig. 2l–n). Disrupting the poison exon's 3'ss and/or ESE with CRISPR-directed mutagenesis dramatically increased BRD9 protein in *SF3B1*-mutant UVM cells (Fig. 2d, Extended Data Fig. 2o, Supplementary Table 8), but had no effect on *BRD9* splicing or expression in *SF3B1*-WT cells (Extended Data Fig. 2p–r).

Several studies recently described BRD9 as part of ncBAF, which is biochemically distinct from canonical BAF (cBAF) and polybromo-associated BAF (PBAF)[5–7] (Fig. 3a). Although ncBAF is not recurrently mutated in cancer—unlike cBAF and PBAF (Extended Data Fig. 3a)—our data suggested that ncBAF is nonetheless frequently disrupted via *SF3B1* mutations.

We investigated the consequences of BRD9 loss by *SF3B1* mutations for ncBAF function. Immunoprecipitation and mass spectrometry to identify BRD9's chromatin-associated interaction partners in K562 cells specifically recovered ncBAF components (Extended Data Fig. 3b–c, Supplementary Table 9). We confirmed these results by immunoblotting against shared and complex-specific components of cBAF, PBAF, and ncBAF in K562 and UVM cells (Fig. 3b, Extended Data Fig. 3d). Expression of mutant, but not WT, SF3B1 reduced BRD9 protein levels and abolished BRG1-GLTSCR1 interactions while leaving BRG1-BAF155 interactions intact, indicating that SF3B1 mutations specifically perturb ncBAF

rather than disrupting all BAF complexes (Fig. 3c, Extended Data Fig. 3e). Chemical degradation of BRD9 (dBRD9)[19] or *BRD9* knockout similarly reduced BRG1-GLTSCR1 interaction (Fig. 3c, Extended Data Fig. 3f). We next identified BRD9 domains necessary for ncBAF formation by generating 3xFLAG-BRD9 deletion mutants and testing for interactions with GLTSCR1/1L. These experiments revealed that BRD9's DUF3512 domain mediates its interaction with GLTSCR1/1L (Extended Data Fig. 3g–h).

We next determined how *SF3B1* mutations altered ncBAF localization to chromatin. We mapped genome-wide binding of the pan-BAF component BRG1 and ncBAF-specific components BRD9 and GLTSCR1 in MEL270 cells expressing WT or mutant SF3B1. We additionally performed the same ChIP-seq experiments following treatment with DMSO or dBRD9 in order to identify BRD9-dependent effects. BRD9 and GLTSCR1 exhibited significant co-localization, consistent with their mutual requirement for ncBAF formation, and were found at a subset of the loci bound by BRG1 (Fig. 3d). BRD9 and GLTSCR1 bound promoters, gene bodies, and likely enhancers, with focal binding at promoters relative to BRG1 (Fig. 3e, Extended Data Fig. 4a). CTCF motifs exhibited striking co-localization with GLTSCR1, but only modest co-localization with BRG1 (Fig. 3f, Extended Data Fig. 4b).

We then tested how depletion of BRD9 (induced by *SF3B1*K700E or dBRD9) altered ncBAF localization. We defined the genomic loci bound by GLTSCR1 in all samples as constitutive sites. Conversely, we defined genomic loci bound by GLTSCR1 in both control (WT *SF3B1* or DMSO) but not BRD9-depleted (mutant SF3B1 or dBRD9) samples as BRD9-sensitive sites (Extended Data Fig. 4c). GLTSCR1 peaks were more BRD9-sensitive than BRG1 peaks and CTCF motifs were uniquely enriched in BRD9-sensitive loci ($p <$ 10^{-8}) versus constitutive GLTSCR1-bound loci (Extended Data Fig. 4d). CTCF was similarly highly enriched at BRG1-bound loci that were BRD9-sensitive ($p < 10^{-55}$; Extended Data Fig. 4e–f). We conclude that BRD9 loss induced by *SF3B1* mutations causes specific loss of ncBAF at CTCF-associated loci.

We identified genes with BRD9-sensitive ncBAF binding in their promoters or enhancers to find that BRD9 loss in UVM preferentially affected genes involved in apoptosis and cell growth, adhesion, and migration (Extended Data Fig. 4g). To understand how BRD9 loss altered gene expression, we identified genes whose promoters exhibited BRD9-sensitive ncBAF binding and which were differentially expressed in *SF3B1*-mutant versus WT UVM patients. Loss of ncBAF binding was associated with promotion as well as repression of gene expression, suggesting that ncBAF, like other SWI/SNF complexes, plays both activating and repressive roles[20] (Extended Data Fig. 4h–j).

Several recent studies reported that BRD9 is required for the survival of certain cancers, particularly those with mutations affecting PBAF and cBAF[6,16,21]. Because *BRD9* loss conferred a proliferative advantage to cancer types with recurrent *SF3B1* mutations (Fig. 1d, Extended Data Fig. 1), we wondered whether normalizing BRD9 levels might suppress growth of *SF3B1*-mutant cells.

As *SF3B1* is recurrently mutated in uveal (Fig. 4a), mucosal, and cutaneous melanomas, we first tested whether *BRD9* loss induced melanomagenesis *in vivo*. We transduced non-tumorigenic murine melanocytes (Melan-a cells), which require oncoprotein expression for sustained growth, with a non-targeting shRNA (Extended Data Fig. 5a), doxycycline (dox)-inducible shRNAs targeting *Brd9* or *Brg1*, or a cDNA encoding the oncoprotein CYSLTR2 L129Q (positive control[22]). KD of either *Brd9* or *Brg1* resulted in potent tumor growth, augmented melanocyte pigmentation, and expression of melanocyte lineage-specific genes *in vivo* (Fig. 4b–c, Extended Data Fig. 5b–g).

We next tested whether *Brd9* expression influenced metastasis. *Brd9* KD significantly increased the number of pulmonary metastatic foci following intravenous injection of murine melanoma (B16) or human UVM (92.1) cells into mice (Extended Data Fig. 6a–f). In contrast, restoring *Brd9* expression in established tumors *in vivo* by withdrawing doxycycline suppressed tumor growth (Extended Data Fig. 6g–h). Similarly, ectopic expression of full-length BRD9, but not the bromodomain or DUF3512 deletion mutants, suppressed growth of UVM cell lines and xenografts (Fig. 4d–e, Extended Data Fig. 6i–k). These data demonstrate that *Brd9* loss promotes cell transformation, tumor maintenance, and metastatic progression, and that BRD9's bromodomain and DUF3512 domain are essential for its anti-proliferative effects.

We sought to understand how BRD9 loss promotes melanoma tumorigenesis. We identified BRD9-bound genes that exhibited dysregulated expression in *SF3B1*-mutant versus WT UVM patient samples and isogenic UVM cells with or without mutant SF3B1 and with or without forced BRD9 loss. *HTRA1*, a known tumor suppressor in melanoma[23,24], was the most down-regulated gene in UVM (Extended Data Fig. 7a–c). HTRA1 was suppressed by mutant SF3B1 expression and dBRD9 treatment of *SF3B1*-WT UVM cells, while mutagenesis of the *BRD9* poison exon increased HTRA1 levels in *SF3B1*-mutant UVM cells (Extended Data Fig. 7d–e). *HTRA1* is bound by ncBAF in UVM and this binding is reduced by mutant SF3B1 (Extended Data Fig. 7f). *HTRA1* KD promoted growth of *SF3B1*-WT UVM, while ectopic *HTRA1* expression suppressed growth of *SF3B1*-mutant UVM (Extended Data Fig. 7g–k). These data suggest that perturbation of ncBAF-dependent regulation of *HTRA1* contributes to the pro-tumorigenic effects of BRD9 loss.

We next tested whether correcting *BRD9* mis-splicing suppressed tumorigenesis. CRISPR-based mutagenesis of the poison exon markedly slowed the growth of *SF3B1*-mutant, but not WT, cells *in vitro* and *in vivo* (Fig. 2d, 4f–g, Extended Data Fig. 2o–r, 8). We then designed ASOs to block *BRD9* poison exon inclusion (Fig. 4h, Extended Data Fig. 9a). We treated *SF3B1*-mutant cells with a non-targeting (control) or poison exon-targeting ASO and measured *BRD9* splicing, BRD9 protein, and cell growth. Each targeting ASO prevented poison exon inclusion, increased BRD9 protein levels, and suppressed cell growth relative to the control ASO (Fig. 4h, Extended Data Fig. 9b). The relative abilities of each ASO to restore BRD9 protein and suppress cell growth were strongly correlated, consistent with on-target effects.

We next tested whether ASO treatment slowed tumor growth *in vivo*. We treated *SF3B1*-mutant (MEL202-derived) xenografts with each ASO via intratumoral injection for 16 days.

Treatment with the poison exon-targeting, but not non-targeting, ASO corrected *BRD9* mis-splicing, significantly reduced tumor growth, and induced tumor necrosis (Fig. 4i–j, Extended Data Fig. 9c–f). We observed similar ASO efficacy in a rectal melanoma patient-derived xenograft (PDX) with *SF3B1*R625C (Fig. 4k, Extended Data Fig. 9g–i, Supplementary Table 7). In contrast, when we performed an identical experiment with a UVM PDX lacking an *SF3B1* mutation, treatment with the poison exon-targeting ASO had no effect (Extended Data Fig. 9j–l, Supplementary Table 7). We conclude that correcting *BRD9* mis-splicing restores BRD9's tumor suppressor activity in *SF3B1*-mutant cancers.

Although *BRD9* poison exon recognition requires mutant SF3B1, BRD9 mis-splicing and ncBAF disruption may also play roles in *SF3B1*-WT cancers. We identified significant pan-cancer expression correlations between *BRD9* and many genes encoding RNA-binding proteins, as well as six additional *BRD9* NMD isoforms that are expressed in *SF3B1*-WT cancers and predictive of *BRD9* expression (Supplementary Table 10, Extended Data Fig. 10). A recent study also identified a promoter polymorphism associated with decreased *GLTSCR1* expression as a common risk allele for AML[25].

As we observed *BRD9* mis-splicing in diverse cancers carrying distinct *SF3B1* mutations, targeting *BRD9* mis-splicing could be a productive pan-cancer therapy. Although ASO treatment merely restored BRD9 mRNA and protein to normal levels, we nonetheless observed strong suppression of tumor growth. The functional impact of correcting *BRD9* mis-splicing was particularly notable given that the UVM models used here contain hundreds of other mis-splicing events and multiple pro-tumorigenic mutations. Given the recent clinical successes with treating spinal muscular atrophy and other diseases with ASOs[26], the tumor-suppressive effects of correcting *BRD9* mis-splicing suggest that oligonucleotide-based therapy may prove similarly promising for treating cancers with spliceosomal mutations.

METHODS

No statistical methods were used to predetermine sample size. The experiments were not randomized. The investigators were not blinded to allocation during experiments and outcome assessment.

Cell lines and tissue culture.

All cell lines underwent short-tandem repeat (STR) testing (ATCC) and MSK IMPACT genetic analysis[28] to evaluate for spliceosome gene mutational status and status of recurrently mutated genes in cancer. HEK293T cells were grown in DMEM/10% FCS. Ba/F3 cells and Melan-a cells (provided by Dorothy Bennett) were grown in RPMI/10% with 1 ng/ml IL-3 (PeproTech; 213-13) and 200 nM TPA (Sigma-Aldrich), respectively, unless noted otherwise. The K562 and NALM-6 isogenic cell lines (engineered to express *SF3B1*K700E, *SF3B1*K666N, or *SF3B1*K700K from the endogenous *SF3B1* locus) were cultured in RPMI/10% FCS and their generation has been described previously[29]. MEL270, MEL285, RN2 cell lines were cultured in RPMI/10% FCS. MEL202, 92-1, and SK-MEL30 cells were grown in RPMI/10% FCS/1% GlutaMAX (Gibco). UPMD1 and UPMD2 cells were grown in Ham F-12/10% FCS. CFPAC1 cells were cultured in IMDM/10% FCS. KPC,

Miapaca2, B16 cells were cultured in DMEM/10% FCS. Panc 05.04 cells were grown in RPMI/20% FCS/20 Units/ml human recombinant insulin. T47D cells were cultured in RPMI1640 supplemented with 10% fetal bovine serum (Corning), 100 μg/mL penicillin, 100 mg/mL streptomycin (Corning), and 4 mM glutamine. All cell culture media include penicillin (100 U/ml) and streptomycin (100 μg/ml).

Primary human samples and human PDX models.

Studies were approved by the Institutional Review Boards of Memorial Sloan Kettering Cancer Center (MSK), informed consent was obtained from all subjects (under MSK IRB protocol 06-107) and conducted in accordance to the Declaration of Helsinki protocol. Patients provided samples after their informed consent and primary human de-identified CLL samples derived from whole peripheral blood or BM mononuclear cells were utilized. PDX models were performed using tumor biopsies from de-identified patients under MSK IRB protocol 14-191. Genomic alterations in melanoma tumor biopsies and CLL cells were analyzed using MSK IMPACT[28] assay or FoundationOne Heme[30] assay, both as previously described. Patient samples were anonymized by the Hematologic Oncology Tissue Bank of MSK (for CLL samples) and the MSK Antitumor Assessment Core Facility (for PDX samples).

Animals.

All animals were housed at Memorial Sloan Kettering Cancer Center (MSKCC). All animal procedures were completed in accordance with the Guidelines for the Care and Use of Laboratory Animals and were approved by the Institutional Animal Care and Use Committees at MSKCC. All mouse experiments were performed in accordance with a protocol approved by the MSKCC Institutional Animal Care and Use Committee (11-12-029). SCID animals (Jackson laboratories stock #001303) were used for all human cell line xenografts while NSG mice (Jackson laboratories stock #005557) were used for patient-derived xenografts (PDX). For all mouse experiments, the mice were monitored closely for signs of disease or morbidity daily and were sacrificed for visible tumor formation tumor volume >1 cm^3, failure to thrive, weight loss>10% total body weight, open skin lesions, bleeding, or any signs of infection. In none of the experiments were these limits exceeded.

HA tag knockin into endogenous *BRD9*.

The following guide RNA sequence targeting *BRD9* transcriptional start site was selected using the Optimized CRISPR Design tool (http://crispr.mit.edu): CGAGTGGCGCTCGTCCTACG. DNA oligonucleotides were purchased from IDT and cloned into px458-GFP vector. For homologous recombination, we purchased a custom IDT Ultramer 197bp repair template (single strand donor DNA) with the HA sequence (TACCCATACGATGTTCCAGATTACGCT) directly following the BRD9 start codon. This 197bp fragment contained two silent mutations, one to remove the PAM site (AGG>AAG) and another to introduce an XhoI restriction enzyme (CTCGGG >CTCGAG) site upstream of the HA tag. The 197bp fragment also contained 83bp of homology to BRD9 5' UTR upstream of the HA tag and 87bp of homology to the BRD9 exon1 downstream of the start codon. Five ug of the targeting construct and 500nM repair template were nucleofected into

K562 *SF3B1*K700E cells and MEL270 cells using the Lonza Nucleofector V kit and Program T-003 on the Nucleofector device. Nucleofected cells were single cell sorted based on GFP positivity 48-hours following nucleofection. Clones were screened for the presence of successful HA insertion by *BRD9* exon 1 PCR and subsequent restriction enzyme digest with XhoI and direct Sanger sequencing. A single positive clone containing the HA coding sequencing was selected to carry out further studies. sgRNAs: CACCCGAGTGGCGCTCGTCCTACG (top), AAACCGTAGGACGAGCGCCACTCG (bottom) Single strand donor DNA: CCAGGGGGCGGTGGCGGCCAAGGTCCGACCGGGTGCCAGCTGTTCCCAGCCCCC GCCTCGAGCCCGCCGCCGGCGCCGCCATGTACCCATACGATGTTCCAGATTACGCT GGCAAGAAGCACAAGAAGCACAAGGCCGAGTGGCGCTCGTCCTACGAAGGTGAG GCGGCGGCGCTTTGTGACGCGCGGCGGGCGGGG PCR primers - Fwd: AGCGAGCTCGGCAACCTCG, Rev: CTTCAGGACTAGCTTTAGAGGC Sanger Sequence primers – Rev: TGCAGCCTCGAACCCAGAAC

Overexpression of SF3B1 cDNA in K562 cells.

2 µg of PiggyBac Transposase construct (CMV-PB-Transposase-IRES-TK-HSV), and 6 µg of *SF3B1*[WT] (ITR-CAG-Flag-*SF3B1*WT-IRES-Puro-ITR) or *SF3B1*[K700E] mutant (ITR-CAG-Flag-*SF3B1*K700E-IRES-Puro-ITR) cDNA constructs were electroporated into 2×10^6 cells (in 200 µL volume) using the Amaxa Nucleofector Protocol (Program T-003) according to manufacturer instructions (Lonza). Puromycin selection (1 µg/mL) was initiated 4 days after electroporation to select for cells that successfully incorporated the constructs. Sanger sequencing was performed to confirm successful integration of the cDNA plasmid using the following primers – Fwd: TCCAATCAAAGATCTTCTTCCAA, Rev: GAGCAGGTTTCTGCAACGAT.

RT-PCR and quantitative RT-PCR (qRT-PCR).

Total RNA was isolated using RNeasy Mini or Micro kit (Qiagen). For cDNA synthesis, total RNA was reverse transcribed to cDNA with SuperScript VILO cDNA synthesis kit (Life Technologies). The resulting cDNA was diluted 10-20 fold prior to use. Quantitative RT-PCR (qRT-PCR) was performed in 10 µL reactions with either SYBR Green PCR Master Mix. All qRT-PCR analysis was performed on an Applied Biosystems QuantStudio 6 Flex Cycler (ThermoFisher Scientific). Relative gene expression levels were calculated using the comparative CT method. Primers used in RT-PCR reactions were:

BRD9 (human) –	Fwd: GCAATGACATACAATAGGCCAGA, Rev: GAGCTGCCTGTTTGCTCATCA
Brd9 (mouse) –	Fwd: TTGGAGATGGAAGTCTGCTCT, Rev: GCAACTTGCTAGACAGTGAACT
BRD9 poison exon (human) –	Fwd: AGCTCTGTTCTGGAGTTCATG, Rev: CTGAAGAAACTCATAGGGGTCGTG
Brd9 poison exon (mouse) –	Fwd: GGCCCTGTTCTGGACTTCATG, Rev: CTGAAGGAATTCATAAGGGTCGTG
BRD9 poison exon inclusion for siRNA experiment (human) –	Fwd: CAGCAGCTCTGTTCTGGAGT, Rev: CCTGAAAGAAACCAGAGAGCTG

BRD9 poison exon exclusion for siRNA experiment (human) –	Fwd: CAGCAGCTCTGTTCTGGAGT, Rev: TCACCTTCCCCAGAGAGCTG
EPB49 cassette exon inclusion (human) –	Fwd: GCCTGCAGAACGGAGAGG, Rev: ACCACTAGCATTTCATAGGGATAGATCT
EPB49 cassette exon exclusion (human) –	Fwd: GCCTGCAGATCTATCCCTATGAAAT, Rev: CTCAAGCCGCATCCGATCC
BRD9 poison exon for mRNA half-life experiment (human) –	Fwd: GTTGGGGACACCCTAGGAGA, Rev (exclusion specific): CTTCACCTTCCCCAGAGAGC, Rev (inclusion specific): CCCTGAAAGAAACCAGAGAGC
18s rRNA (human) –	Fwd: CTACCACATCCAAGGAAGCA, Rev: TTTTTCGTCACTACCTCCCCG
Mitf (mouse) –	Fwd: CCAACAGCCCTATGGCTATGC, Rev: CTGGGCACTCACTCTCTGC
Dct (mouse) –	Fwd: GTCCTCCACTCTTTTACAGACG, Rev: ATTCGGTTGTGACCAATGGGT
Pmel (mouse) –	Fwd: GAGCTTCCTTCCCGTGCTT, Rev: TGCCTGTTCCAGGTTTTAGTTAC
Tyrp1 (mouse) –	Fwd: CCCCTAGCCTATATCTCCCTTTT, Rev: TACCATCGTGGGGATAATGGC
GAPDH (human) –	Fwd: GGAGCGAGATCCCTCCAAAAT, Rev: GGCTGTTGTCATACTTCTCATGG
Gapdh (mouse) –	Fwd: AGGTCGGTGTGAACGGATTTG, Rev: TGTAGACCATGTAGTTGAGGTCA

mRNA stability assay.

For mRNA half-life measurement using qRT-PCR, anti-*UPF1* shRNAs and control shRNA infected K562 and NALM-6 cells with isogenic *SF3B1*K700E mutations were treated with 2.5 µg/ml Actinomycin D (Life Technologies) and harvested at 0, 2, 4, 6, and 8 hr (using methods as described previously[31]). *BRD9* poison exon inclusion/exclusion and *18s* rRNA mRNA levels were measured by qRT-PCR.

Western blotting.

For western blotting, the following antibodies to the following proteins were used: BRD9 (Bethyl Laboratories; A303-781A and Active Motif; 61538), SF3B1/Sap-155 (MBL; D221-3), Flag-M2 (Sigma-Aldrich; F-1084), β-actin (Sigma-Aldrich; A-5441), GLTSCR1 (Santa Cruz Biotechnology; sc-515086), GLTSCR1L (Thermo Fisher Scientific; PA5-56126), BRM (Bethyl Laboratories; A303-015A), BRG1 (Santa Cruz Biotechnology; sc-17796), BAF155 (Santa Cruz Biotechnology; sc-48350), BAF60A (Santa Cruz Biotechnology; sc-135843), BAF47 (Santa Cruz Biotechnology; sc-166165), ARID1A (Santa Cruz Biotechnology; sc-373784), ARID2 (Santa Cruz Biotechnology; sc-166117), BRD7 (Thermo Fisher Scientific; PA5-49379), U2AF2 (Bethyl Laboratories; A303-665A), U2AF1 (Bethyl Laboratories; A302-080A), Histone H3 (Abcam; ab1791), HTRA1 (R&D systems; MAB2916-SP). All primary antibodies for western blotting were diluted to a final concentration of 1:500 to 1,000, in either 5% BSA (Sigma-Aldrich) in 0.05% TBS-Tween 20 (TBS-T) or 5% skim milk in 0.05% TBS-T. Nuclear extracts were quantified using BCA and 1 mg protein (1 mg ml−1 in IP buffer supplemented with protease inhibitors) was used per immunoprecipitation. Proteins were incubated for 3 hours with 2-5 µg of antibody or with Protein A/G PLUS-Agarose (Santa Cruz Biotechnology; sc-2003) with rotation at 4 °C.

After washing 3 times with Pierce™ IP Lysis Buffer (Thermo Fisher Scientific; 87787), immunoprecipitated proteins were eluted with Pierce™ Lane Marker Reducing Sample Buffer (Thermo Fisher Scientific; 39000) and loaded onto 4-12% Bis-Tris NuPAGE Gels (Life Technologies).

Chromatin immunoprecipitation (ChIP).

For ChIP-seq studies in MEL270 cells, antibodies to endogenous BRG1 (Abcam EPNCIR111A, Lot # GR3208604-8), GLTSCR1 (Santa Cruz SC-240516, Lot # A2313), and BRD9 (Abcam, ab137245) were used and ChIP was performed as described in detail previously[6]. MEL270 cells transduced with empty vector, doxycycline inducible SF3B1 wild type cDNA, or doxycycline inducible SF3B1 K700E mutant cDNA in the backbone of pInducer20, were treated with doxycycline (1 μg/ml) plus dBRD9[19] (250nM) or DMSO for 72 hours before cross-linking.

Mass spectrometry.

For anti-FLAG-BRD9 ChIP followed by mass spectrometry, K562 cells transduced with empty vector or 3xFLAG tagged BRD9 were grown in RPMI/10% FCS. Ten million cells were crosslinked according to the manufacturer's instruction (Active Motif) and as described previously.[32] Cells were fixed with 1% methanol-free formaldehyde (Sigma, F-8775) for 8 min and quenched with 0.125 M glycine (Sigma, G-7403). Chromatin was isolated by the addition of lysis buffer, followed by disruption with a Dounce homogenizer. Lysates were sonicated and the DNA sheared to an average length of 300-500 bp. Genomic DNA (Input) was prepared by treating aliquots of chromatin with RNase, proteinase K and heat for reverse crosslinking, followed by ethanol precipitation. Pellets were resuspended and the resulting DNA was quantified on a NanoDrop spectrophotometer. Extrapolation to the original chromatin volume allowed quantitation of the total chromatin yield. An aliquot of chromatin (150 ug) was precleared with protein G agarose beads (Invitrogen). Proteins of interest were immunoprecipitated using 15 ug of antibody against FLAG and protein G magnetic beads. Protein complexes were washed and trypsin was used to remove the immunoprecipitate from beads and digest the protein sample. Protein digests were separated from the beads and purified using a C18 spin column (Harvard Apparatus). The peptides were vacuum dried using a SpeedVac. Digested peptides were analyzed by LC-MS/MS on a Thermo Scientific Q Exactive Orbitrap Mass spectrometer in conjunction with a Proxeon Easy-nLC II HPLC (Thermo Scientific) and Proxeon nanospray source.

Protein identifications were accepted if they contained at least one identified peptide. Proteins that contained similar peptides and could not be differentiated based on MS/MS analysis alone were grouped to satisfy the principles of parsimony. Proteins sharing significant peptide evidence were grouped into clusters. Protein coverage percentage is observed in the raw data file. Final list generation was done by taking all proteins with a spectral count of five and above from each replicate reaction and comparing them in a venn diagram against IgG control replicates. Proteins unique to both experimental replicates were then applied to the PANTHER database for protein ontology results.

shRNA experiments.

Cells were transduced with a doxycycline-inducible LT3GEPIR lentiviral vector, T3G-GFP-mirE-PGK-Puro-IRES-rtTA3[33], expressing shRNAs for BRD9 or a non-targeting renilla. Short hairpins were induced with the addition of doxycycline (2.0 μg/mL; Sigma Aldrich). All shRNAs were designed using the SplashRNA algorithm (Pelossof et al., 2017). The short hairpin sequences are:

shBRD9-1 (human, shBRD9_352): TTTATTATCATTGAATATCCAG

shBRD9-2 (human, shBRD9_353): TTTTATTATCATTGAATATCCA

shBrd9-1 (mouse, shBrd9_511): TTTATTATCATTGAATACCCAG

shBrd9-2(mouse, shBrd9_512): TTTTATTATCATTGAATACCCA

shHTRA1-1 (human, shHTRA1_1192): TTTTTAATCTTATCAGATGGGA

shHTRA1-2 (human, shHTRA1_1669): TGAACAAACAAAATGGCAGTCA

shHTRA1-3 (human, shHTRA1_1898): TTCTATCTACGCATTGTATCGA

siRNA transfections.

K562 cells were transfected with a non-targeting control siRNA (Dharmacon, D-001810-01, target sequence: UGGUUUACAUGUCGACUAA), a siRNA pool against *U2AF1* (Dharmacon ON-TARGETplus SMARTpool, L-012325-01), or a siRNA pool against *U2AF2* (Dharmacon ON-TARGETplus SMARTpool, L-012380-02) using the Nucleofector II device from Lonza with the Cell Line Nucleofector Kit V (program T16). RNA and protein were extracted 48 hours post-transfection. cDNA was produced using 1 μg of RNA and the Superscript III first strand synthesis system (Thermo Fisher, 18080051).

***In vitro* competition assay.**

For competition assay to evaluate the cellular effect of sgBRD9/Brd9, cell lines were transduced with LentiCas9-Blast (Addgene; #52962) and then single-cell sorted into 96-well plates. Among these clones, we used single clones with strong Cas9 expression, which was confirmed by Western blotting. Cas9 expressing cells were lentivirally transduced with iLenti-guide-GFP vectors subcloned with the gRNA sequences below in which sgRNA expression was linked to GFP expression. The percentage of GFP-expressing cells was then measured over time after infection using BD LSRFortessa. GFP positive rate in living cells at each point compared to that of day2 were calculated. Similarly, to evaluate the cellular effect of BRD9 fragment cDNA, HTRA1 cDNA, or shRNAs against BRD9 or HTRA1, GFP positive rates were followed up after transducing pMIGII-backbone plasmids (cDNA) and LT3GEPIR plasmids (shRNA), respectively, into melanoma cell lines.

sgBRD9-1 (human): ACTCCAGTTACTATGATGAC, sgBRD9-2 (human): AGAGAGGGAGCACTGTGACA, sgBRD9-3 (human): AGATACCGTGTACTACAAGT, sgBrd9-1 (mouse): ATTAACCGGTTTCTCCCGGG, sgBrd9-2 (mouse):

GGAACACTGCGACTCAGAGG, sgBrd9-3 (mouse): ACTTGCTAGACAGTGAACTC, Control (Scrambled): ACGGAGGCTAAGCGTCGCAA

CRISPR enrichment screening for NMD targets.

First, Ba/F3 cells were transduced with LentiCas9-Blast (Addgene; #52962) and single-cell sorted into 96-well plates. Among these clones, we used a single clone with strong Cas9 expression. sgRNA library of NMD targets in SF3B1 mutant cells were amplified and packaged as lentivirus. The library includes 4 sgRNAs against each target gene (274 genes), 100 control sgRNAs, and positive control sgRNAs against Pten. Ba/F3 cells were transduced with lentivirus carrying sgRNA library produced by 293FT cells and puromycin selection (2 μg/ml) was performed in IL-3-containing media for 7 days. Then, we washed out IL-3 (Day0) and the surviving cells were harvested at 7 days after IL-3 depletion (Day 7). Cell pellets were lysed and genomic DNA was extracted (Qiagen) and quantified by Qubit (ThermoScientific). A quantity of gDNA covering 1,000X representation of gRNAs was PCR amplified using Q5 high-fidelity polymerase (NEB cat# M0491) to add Illumina adapters and multiplexing barcodes. Amplicons were quantified by Qubit and Bioanalyzer (Agilent) and sequenced on Illumina HiSeq 2500. Sequencing reads were aligned to the screened library; counts were computed for each gRNA; counts for each sgRNA were compared between days 0 and 7 after cytokine depletion. For the probe-level analysis, we fitted a negative binomial generalized log-linear model and performed a likelihood ratio test with glmFit and glmLRT in the R/Bioconductor edgeR package. For the gene-level analysis, we used the CAMERA test as implemented in edgeR[34–36]. FDRs were computed with the Benjamini-Hochberg method.

CRISPR-directed mutations.

Cas 9 expressing MEL202 and MEL270 cells were transduced with iLenti-guide-Puro vector targeting 5' end of BRD9 poison exon. sgRNA used to induce mutations was: AAAATACTCAGTTTCTTTCA. Single cell sorting was performed into 96 well plate by BD FACSAria™ III cell sorter after puromycin selection (2.0 μg/mL for 7 days). The mutations caused by Cas9 and sgRNA were confirmed by PCR amplification followed by Sanger sequencing.

PCR primers - Fwd: TGTTGGGTCAGGAAGAGACTTG, Rev: CCATGGACTGAACGGATTCC

Sanger sequencing primer – Fwd: TGTTGGGTCAGGAAGAGACTTG

Colony forming assays.

Single-cell suspensions were prepared from MEL202 and MEL270 cells with or without CRISPR mediated indel and 3,000 cells from each were plated in triplicates in 6-well treated plates, and colonies were enumerated 10 days later. After 10 days, colonies were fixed with 3.7% paraformaldehyde for 5 minutes and stained in a solution of 0.05% crystal violet for 30 minutes at room temperature and washed in PBS and tap water.

In vitro cell viability assays.

Cells were seeded in white flat-well 96-well plates (Costar) at a density of 1000 cells per well. ATP luminescence readings were taken every 24h after seeding using Cell Titer Glo (Promega) according to the manufacturer's instructions.

BRD9 minigene assay.

We identified putative ESEs with SpliceAid2[37]. We used SF3B1 wild-type MEL270 and T47D cells transduced with FLAG-SF3B1 WT or FLAG-SF3B1K700E cDNA (in the backbone of pInducer20 (Addgene, #44012)). After drug selection with Neomycin (Thermo Fisher Scientific, 10131027), the selected cells were treated with 1 μg /ml doxycycline (Sigma, D9891). The *BRD9* minigene construct was generated by inserting the DNA fragment containing the *BRD9* genomic sequence from exon 14 to exon 15 in between the BamHI and AgeI restriction sites in the FRE5 plasmid (Addgene 62377) via Gibson assembly. *BRD9* minigene mutagenesis was performed with the Agilent QuikChange II Site-directed mutagenesis kit with specific primers according to the manufacturer's directions. For transient transfection experiments, cells were seeded into 24-well plate one day before transfection of *BRD9* minigene constructs in the presence of X-tremeGENE HP DNA transfection reagent (Roche) according to the manufacturer's directions. Forty-eight hours after transfection, cells were harvested and RNA was extracted using Qiagen RNeasy mini kit. Minigene-derived and endogenous BRD9 transcripts were analyzed by RT-PCR using specific primers. Primers and oligonucleotides used in RT-PCR reactions were:

Cloning –	Fwd: GGACCCAGTACCAGGATCCGTTGGGGACACCCTAGGAG, Rev: CTTGGAGGAGCGCACACCGGTCAGGTGGTGCTGGTCCCTC
RT-PCR–	Fwd (minigene): GGATTACAAGGATGACGATGAC, Fwd (endogenous): CATGAAGCCTCCAGATGAAG, Rev (common): CTTCGTCGTCTCATCCAAGTTC
Mutagenesis (AAAA to TTTT) –	Fwd: CAAAGGGATATATTTTGAGATTTTTTACTCAGTTTCTTTCAGG, Rev: CCTGAAAGAAACTGAGTAAAAAATCTCAAAATATATCCCTTTG
Mutagenesis (AAAA to ATAT) –	Fwd: CAAAGGGATATATTTTGAGATATATTACTCAGTTTCTTTCAGG, Rev: CCTGAAAGAAACTGAGTAATATATCTCAAAATATATCCCTTTG
Mutagenesis (GATAAAA to TTTTTTT) –	Fwd: GTCAAAGGGATATATTTTGATTTTTTTTACTCAGTTTCTTTCAGG, Rev: CCTGAAAGAAACTGAGTAAAAAAAATCAAAATATATCCCTTTGAC
Mutagenesis (TTTCT to TTACA at exon 14a)–	Fwd: GAGATAAAATACTCAGTTACATTCAGGGCCTGCCATCTATC, Rev: GATAGATGGCAGGCCCTGAATGTAACTGAGTATTTTATCTC
Mutagenesis (TTTCT to TTGCG at exon 14a)–	Fwd: GAGATAAAATACTCAGTTGCGTTCAGGGCCTGCCATCTATC, Rev: GATAGATGGCAGGCCCTGAACGCAACTGAGTATTTTATCTC
Mutagenesis (TTTCT to TTTCA at exon 14a)–	Fwd: GAGATAAAATACTCAGTTTCATTCAGGGCCTGCCATCTATC, Rev: GATAGATGGCAGGCCCTGAATGAAACTGAGTATTTTATCTC
Mutagenesis (TTTCT to TTTCG at exon 14a)–	Fwd: GAGATAAAATACTCAGTTTCGTTCAGGGCCTGCCATCTATC, Rev: GATAGATGGCAGGCCCTGAACGAAACTGAGTATTTTATCTC
Mutagenesis (TTTCT to TTTAT at exon 14a)–	Fwd: GAGATAAAATACTCAGTTTATTTCAGGGCCTGCCATCTATC, Rev: GATAGATGGCAGGCCCTGAAATAAACTGAGTATTTTATCTC
Mutagenesis (Branch point A to G)–	Fwd: GTCAAAGGGATATATTTTGGGATAAAATACTCAGTTTCTTTC, Rev: GAAAGAAACTGAGTATTTTATCCCAAAATATATCCCTTTGAC

Lariat sequencing.

To map the branchpoints that were used when the *BRD9* poison exon was included or excluded, RT-PCR was performed to amplify branchpoint-spanning fragments from lariat RNAs arising during normal (poison exon exclusion) or aberrant (poison exon inclusion) splicing of BRD9 pre-mRNA. Briefly, SuperScript III reverse transcriptase (Invitrogen) and a primer complementary to the intronic sequences downstream of the 5' splice sites were used to generate cDNA from lariat RNAs. Branchpoint-spanning fragments were then amplified from lariat RNAs by nested PCR with pairs of outer primers (with the RT primer being the reverse primer) and inner primers. The forward primers were complementary to sequences about 200-300 nucleotides upstream of the 3' splice sites and the reverse primers were complementary to sequences downstream of the 5' splice sites (see Supplementary Table 11). The PCR products were cloned into the pGEM-T vector (Promega) and sequenced by Sanger sequencing.

Melanoma transplant model.

We resuspended stably-transduced Melan-a/MEL270/MEL202 cells (1M cells) with doxycycline-inducible shRNAs, cDNAs, or sgRNAs in 100 μl of a 1:1 mix of medium and Matrigel (BD Biosciences) and subcutaneously and bilaterally injected the mix into the flanks of 7-week-old female CB17-SCID mice (Taconic). For doxycycline-regulated shRNA induction, we used doxycycline-containing diets (625mg/kg diet, Envigo). To assess tumor growth, at least five mice per group were injected for a total of ten tumors per group. No randomization or blinding was used in the analysis of tumor growth. Tumors were measured with calipers every 7 days. Growth curves were visualized with Prism GraphPad 8.0. Tumor volume was calculated using the formula; Volume = π(length)(width)(height)/6.

In vitro morpholino transfection.

To deliver morpholinos into cultured cell lines, we followed the manufacturer's instruction (GeneTools LLC). Briefly, we used 6uM Endo-Porter after adding morpholinos (final concentration: 10uM). RNA and proteins are collected 48 hours after delivery.

morpholino target sequence - #3 TAATGAGGCAAGTCCAGTCCCGCTT, #6 AAAGAGGGGATAATGAGGCAAGTCC, #7 GGGATAATGAGGCAAGTCCAGTCCC.

In vivo morpholino treatment.

Treatment with morpholinos was started when the tumor volume in mice reached 100-200 mm³. Cohorts were treated intratumorally with 12.5 mg/kg scrambled or poison exon-targeting Vivo-Morpholinos (AAAGAGGGGATAATGAGGCAAGTCC, GeneTools LLC) dissolved in 50 μl PBS, every 2 days for 8 doses total. The mice were dissected 24 hours after the final treatment. For the PDX model, patients' derived rectal melanoma cells (SF3B1- R625C) and UVM cells (SF3B1 wild type) were serially transplanted into SCID mice and treated similarly.

In vivo metastasis model.

For lung experimental metastasis, B16 and 92.1 melanoma cells retrovirally transduced with shRenilla, shBRD9/Brd9#1 and shBRD9/Brd9#2 in MLS-E vector (sorted using GFP) were trypsinized, resuspended in PBS, and then 0.4M cells in 0.2 mL PBS were injected via the lateral tail vein using a 27-gauge needle. Mice were sacrificed 14 days after injection and tissues were isolated and fixed in 4% paraformaldehyde (Thermo Fisher Scientific). For evaluation of metastatic colonization of the lung using 92.1 human UVM cells, the burden of metastatic cells was evaluated using GFP expression by flow cytometry as well as anti-GFP immunohistochemistry 14 days following tail-vein injection of 0.4M cells into NOD-Scid IL2Rγ null mice.

Histologic analysis.

Tissues were fixed in 4% paraformaldehyde, processed routinely in alcohol and xylene, embedded in paraffin, sectioned at 5-micron thickness, and stained with hematoxylin-eosin (H&E). Immunohistochemistry (IHC) was performed on a Leica Bond RX automated stainer (Leica Biosystems, Buffalo Grove, IL). Following heat induced epitope retrieval at pH 6.0, the primary antibody against Ki67 (Vector VP-K451) were applied, followed by application of a polymer detection system (DS9800, Novocastra Bond Polymer Refine Detection, Leica Biosystems) in which the chromogen was 3,3 diaminobenzidine tetrachloride (DAB) and counterstain was hematoxylin. Photomicrograph examination of all H&E and IHC slides were performed using a Zeiss Axioskop imaging.

BRD9 expression correlates.

cor.test (in R) was used to calculate Spearman's ρ and the associated *p*-value associated with the correlation of *BRD9* expression with the expression of each coding gene across all samples within each TCGA cancer cohort. Analysis was restricted to coding genes not on the same chromosome arm as *BRD9* (chromosome 5p) to remove potential confounding effects of local correlations. Coding genes with $p < 0.01$ in at least 10 cancer types were ranked by their absolute mean value of ρ (computed across all TCGA cohorts) and classified as RNA-binding if they were annotated with the "RNA-binding" Gene Ontology term (GO: 0003723).

BRD9 alternative splicing.

Potential NMD-targeted isoforms of *BRD9* were identified as follows: we queried the MISO v2.0 alternative splicing annotation[38] for exon skipping and competing splice site events within the *BRD9* gene locus, restricted to those events with evidence of alternative splicing based on spliced junction reads identified via the TCGA analysis described below, assigned open reading frames for the isoforms resulting from each alternative splicing event based on the *BRD9* isoform with the longest open reading frame, and classified isoforms as predicted NMD substrates if they contained a termination codon > 50 nt upstream of a splice junction.

Robust linear modeling of *BRD9* expression based on the identified alternatively spliced isoforms of *BRD9* that are predicted NMD substrates was performed for each cancer cohort with the rlm function in the MASS package in R. Relative expression of each isoform in each sample was estimated from RNA-seq data across all TCGA cohorts as described below.

A z-score normalization was performed across all samples for each isoform in each cohort prior to model fitting. The resulting coefficients from the fitted models were subsequently used to predict *BRD9* expression from *BRD9* NMD-targeted isoform expression.

RNA-seq library preparation.

RNA-seq libraries were prepared from TRIzol-isolated (Thermo Fisher catalog no. 15596026) RNA using the Illumina TruSeq RNA Library Prep Kit v2 (Illumina catalog no. RS-122-2001/2). K562 libraries were sequenced at MSKCC with 101 bp single-end reads. MEL270 libraries were sequenced by the FHCRC Genomics Shared Resource with 2x51 bp paired-end reads.

ChIP-seq library preparation.

ChIP-seq libraries were prepared and sequenced as previously described[6] by the Molecular Biology Core Facilities at the Dana-Farber Cancer Institute with 75 bp single-end reads.

Genomic analysis of SWI/SNF complex members from TCGA.

Mutational analysis of genes encoding SWI/SNF complex members was performed as previously described[39].

Genome annotation, RNA-seq read mapping, and gene and isoform expression estimation.

RNA-seq reads were processed for gene expression and isoform ratio quantification as previously described[40]. In brief, RNA-seq reads were aligned to the hg19/GRCh37 assembly of the human genome using a gene annotation created by merging the UCSC knownGene gene annotation[41], Ensembl v71.1 gene annotation[42], and MISO v2.0 isoform annotation[38]. Read alignment and expression estimation were performed with RSEM v1.2.4[43], Bowtie v1.0.0[44], and TopHat v2.1.1[45]. Isoform ratios were quantified with MISO v2.0[38]. Gene expression estimates were normalized by applying the trimmed mean of M values (TMM) method[46] to coding genes. Statistical tests for differential gene and isoform expression were performed for single-sample comparisons with Wagenmakers's Bayesian framework[47] and for sample group comparisons with the Mann-Whitney U test. RNA-seq read coverage plots (e.g., Fig. 1e) represent reads normalized by the number of reads mapping to all coding genes in each sample (per million).

RNA-seq coverage plots.

RNA-seq coverage plots were made using the UCSC Genome Browser[48] and/or the ggplot2 package in R[49]. Repetitive elements were annotated by RepeatMasker[27].

Cluster analysis.

Unsupervised clustering of CLL, MDS, and UVM samples (Fig. 1a) was based on the 40 events that were differentially spliced in isogenic UVM (MEL270 cells) as well as myeloid leukemia (K562 cells) cells expressing *SF3B1* K700E versus WT SF3B1, restricted to the 30 such events with sufficient read coverage in all cohorts for clustering.

ChIP-seq data analysis.

ChIP-seq reads were mapped to the genome by calling Bowtie v1.0.0[44] with the arguments '-v 2 -k 1 -m 1 --best --strata'. Peaks were called using MACS2 v2.1.1.20160309[50] against input control libraries with $p < 10^{-5}$ and subsequently filtered to remove peaks contained within ENCODE blacklisted regions[51] and the mitochondrial genome. Subsequent data analysis was performed with Bioconductor in the R programming environment[52]. Consensus peaks between samples were called using the soGGI package v1.14.0[53]. Peaks were annotated using the ChIPseeker package v1.18.0[54]. Potential transcription factor binding in a 300 nucleotide region around the center of consensus peaks was scored using the TFBSTools package v1.20.0[55], with models taken from the HOCOMOCO v11 human core collection[56] and applied with a threshold of $p < 10^{-4}$. The highest scores for each consensus peak region were collated for each transcription factor. A two-sided Mann-Whitney U test was used to assess the significance of the difference in scores between constitutive and sensitive peaks for each transcription factor.

DATA AVAILABILITY

RNA-seq and ChIP-seq data generated as part of this study were deposited in the Gene Expression Omnibus (accession number GSE124720). RNA-seq data from published studies were downloaded from CGHub (TCGA UVM[57]), EMBL-EBI ArrayExpress (Illumina Human BodyMap 2.0: E-MTAB-513), the Gene Expression Omnibus (accession numbers GSE72790, GSE114922) (CLL: Darman et al. 2015[15], MDS: Pellagati et al. 2018[58]), or directly obtained from the authors (UVM: Alsafadi et al. 2016[10]). Gel source data can be found in Supplementary Fig. 1. Other data that support this study's findings are available from the authors upon reasonable request.

Extended Data
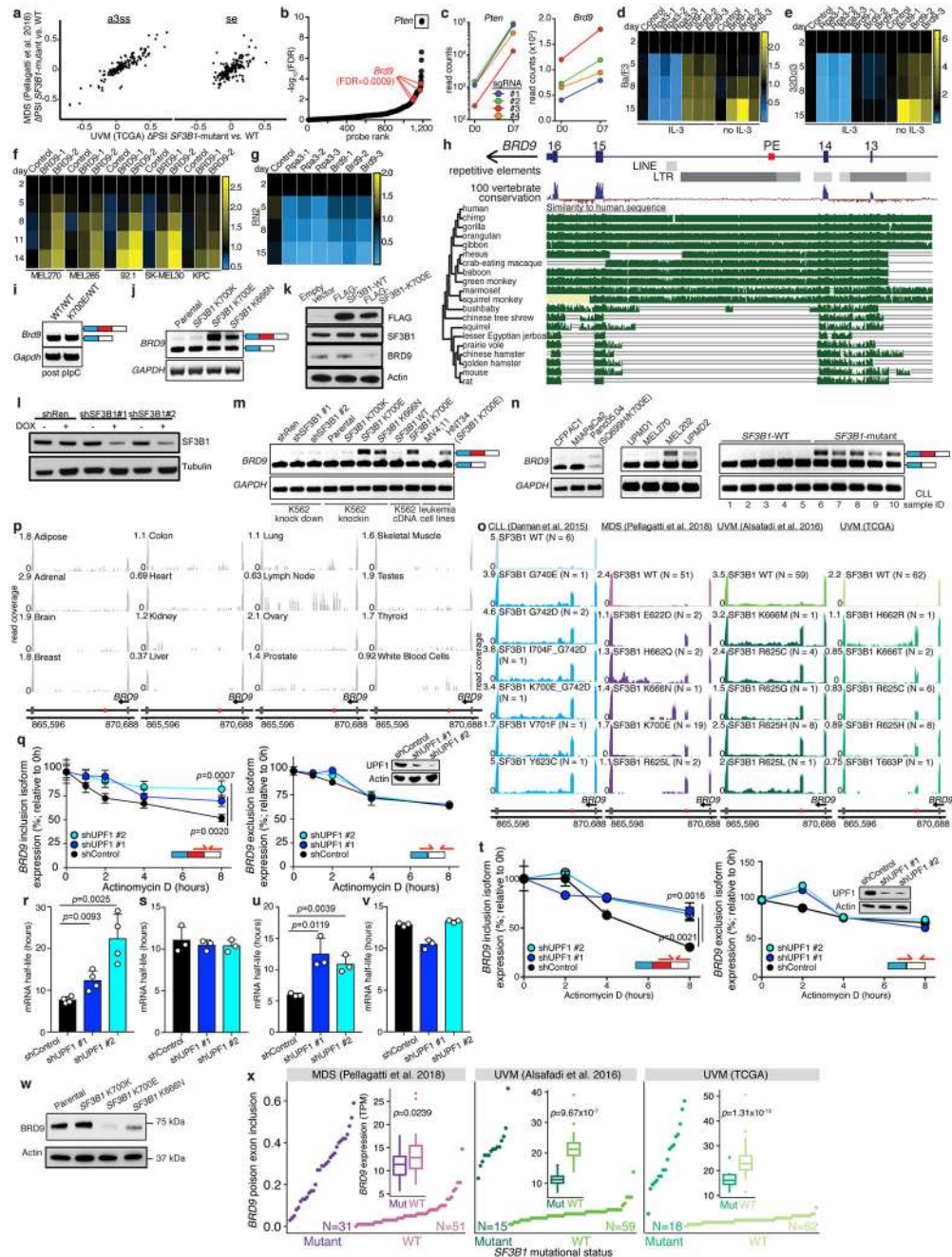
Extended Data Figure 1. ***BRD9* is mis-spliced in *SF3B1*-mutant human cells and BRD9 loss confers a proliferative advantage.**

(**a**) Scatter plots comparing differential splicing (ΔPSI) between *SF3B1*-mutant and WT patients in the TCGA uveal melanoma (UVM) cohort[57] (x axis) and an MDS cohort[58] (y axis). Events were classified as alternative 3' splice sites (a3ss) or skipped exons (se).

(**b**) Rank plot for the −log₁₀(FDR; false-discovery rate) associated with each sgRNA in our CRISPR/Cas9 positive selection screen. sgRNAs targeting the positive control (*Pten*) and *Brd9* are highlighted. For the probe-level (per-sgRNA) analysis, we fitted a negative

binomial generalized log-linear model and performed a likelihood ratio test. FDRs were computed with the Benjamini-Hochberg method.

(**c**) Read counts for sgRNAs targeting the positive control (*Pten*) or *Brd9*. D0 and D7 indicate days following withdrawal of IL-3.

(**d**) Heat map summarizing the results of a competition assay to measure the effect of each indicated sgRNA on the growth of Cas9-expressing Ba/F3 cells. Cell growth was computed with respect to cells treated with a non-targeting (Control) sgRNA and the percentages of GFP$^+$ cells at day 14 were normalized to that at day 2. The illustrated values correspond to the mean computed over n=3 biological replicates. *Rpa3* sgRNAs were used as a negative control.

(**e**) As (**d**), but for 32Dcl3 cells.

(**f**) As (**d**), but for the indicated melanoma and pancreatic ductal adenocarcinoma cells.

(**g**) As (**d**), but for RN2 cells.

(**h**) Sequence conservation of the *BRD9* poison exon locus as estimated by phyloP[60]. Conservation and repetitive element annotation from the UCSC Genome Browser[41]. PE, poison exon.

(**i**) RT-PCR analysis of *Brd9* poison exon inclusion using whole bone marrow cells from *Mx1*-Cre *Sf3b1*$^{WT/WT}$ ("WT/WT") and *Mx1*-Cre *Sf3b1*$^{K700E/WT}$ ("K700E/WT") mice. Three weeks after pIpC treatment, RT-PCR was performed with murine primers corresponding those used to assay *BRD9* poison exon inclusion in human cells. Representative images from n=2 technically independent replicates.

(**j**) RT-PCR analysis to confirm mutant SF3B1-dependent inclusion of the *BRD9* poison exon in isogenic NALM-6 cell lines engineered to contain the indicated mutations. *SF3B1*K700K is a WT control for genome engineering. Representative images from n=2 technically independent replicates.

(**k**) Western blot for FLAG, SF3B1, and BRD9 in K562 cells overexpressing N-terminal FLAG-tagged SF3B1 WT or K700E cDNAs or an empty vector (corresponding to cells evaluated in (**m**)). Representative images from n=2 biologically independent replicates.

(**l**) Western blot for SF3B1 in K562 cells treated with doxycycline-inducible SF3B1-targeting shRNAs or a non-targeting control shRNA ("shRen") (corresponding to cells evaluated in (**m**)). Representative images from n=2 technically independent replicates.

(**m**) RT-PCR illustrating the specificity of *BRD9* poison exon inclusion for *SF3B1*-mutant cells in the indicated cell lines. These include K562 cells treated with control shRNA ("shRen") or SF3B1-targeting shRNAs (columns labeled "K562 knock-down"); knockin of the *SF3B1*K700K, K700E, or K666N mutation into the endogenous locus of *SF3B1* (columns labeled "K562 knockin"); or overexpression of SF3B1 wild-type or SF3B1K700E cDNA (columns labeled "K562 cDNA"). The two right hand-most lanes show acute myeloid leukemia cell lines with wild-type *SF3B1* (MV4:11) or a naturally occurring endogenous *SF3B1*K700E mutation (HNT34 cells; columns labeled "leukemia cell lines"). Representative images from n=3 biologically independent experiments.

(**n**) As (**m**), but for the indicated pancreatic ductal adenocarcinoma cell lines (left), UVM cell lines (center), and a cohort of CLL patients (right). CFPAC1 and MIA PaCa2 cells lack *SF3B1* mutations; Panc05;04 cells carry *SF3B1*Q699H/K700E; UPMD1 and MEL270 cells lack *SF3B1* mutations; MEL202 and UPMD2 cells carry *SF3B1*R625G and *SF3B1*Y623H, respectively. CLL patient sample ID corresponds to genotypes shown in Supplementary

Table 7. Representative images from n=2 technically independent experiments (left and center) and n=3 biologically independent experiments (right).

(**o**) RNA-seq read coverage plots of the *BRD9* poison exon locus from patient samples with the indicated *SF3B1* genotypes. All *SF3B1*-mutant samples exhibit *BRD9* poison exon inclusion.

(**p**) As (**o**), but for the indicated tissues from healthy donors (BodyMap 2.0).

(**q**) Quantitative RT-PCR measurement of the half-lives of the poison exon inclusion (left) and exclusion (right) isoforms in isogenic K562 *SF3B1*K700E cells treated with the indicated shRNAs and actinomycin D to inhibit transcription. NMD inhibition via *UPF1* knockdown stabilizes the inclusion, but not exclusion, isoform. Red arrows indicate primers used to specifically detect the two isoforms. n=2 biologically independent experiments and n=2 technically independent experiments for the inclusion isoform; n=3 technically independent experiments for the exclusion isoform. *p*-value was calculated by two-sided *t*-test at 8h.

(**r**) Bar graph illustrating the estimated poison exon inclusion isoform half-life in the indicated conditions from the data in (**q**). Error bars, mean and SD. n=2 biologically independent experiments and n=2 technically independent experiments. *p*-value was calculated by two-sided *t*-test.

(**s**) As (**r**), but for the exclusion isoform. Error bars, mean and SD. n=3 technically independent experiments. *p*-value was calculated by two-sided *t*-test.

(**t**) As (**q**), but for NALM-6 *SF3B1*K700E cells. n=3 technically independent experiments for the inclusion isoform and the exclusion isoform. *p*-value was calculated by two-sided *t*-test at 8h.

(**u**) As (**r**), but for NALM-6 *SF3B1*K700E cells. n=3 technically independent experiments. Error bars, mean and SD. *p*-value was calculated by two-sided *t*-test.

(**v**) As (**s**), but for NALM-6 *SF3B1*K700E cells. Error bars, mean and SD. n=3 technically independent experiments. *p*-value was calculated by two-sided *t*-test.

(**w**) Western blot for BRD9 in NALM-6 cells with or without knockin of an *SF3B1* mutation. Actin, loading control. Representative images from n=3 biologically independent experiments.

(**x**) Rank plot of *BRD9* poison exon inclusion (scale of 0 to 1; top) and box plot of gene expression (inset) for patients stratified by *SF3B1* mutational status (data are from myelodysplastic syndrome (MDS) and uveal melanoma (UVM) patient cohorts as in Fig. 1a). *SF3B1* mutations were strongly associated with high poison exon inclusion and low *BRD9* expression. Boxes illustrate 1st and 3rd quartiles, with whiskers extending to 1.5X interquartile range. *p*-value computed with one-sided Mann-Whitney U test.
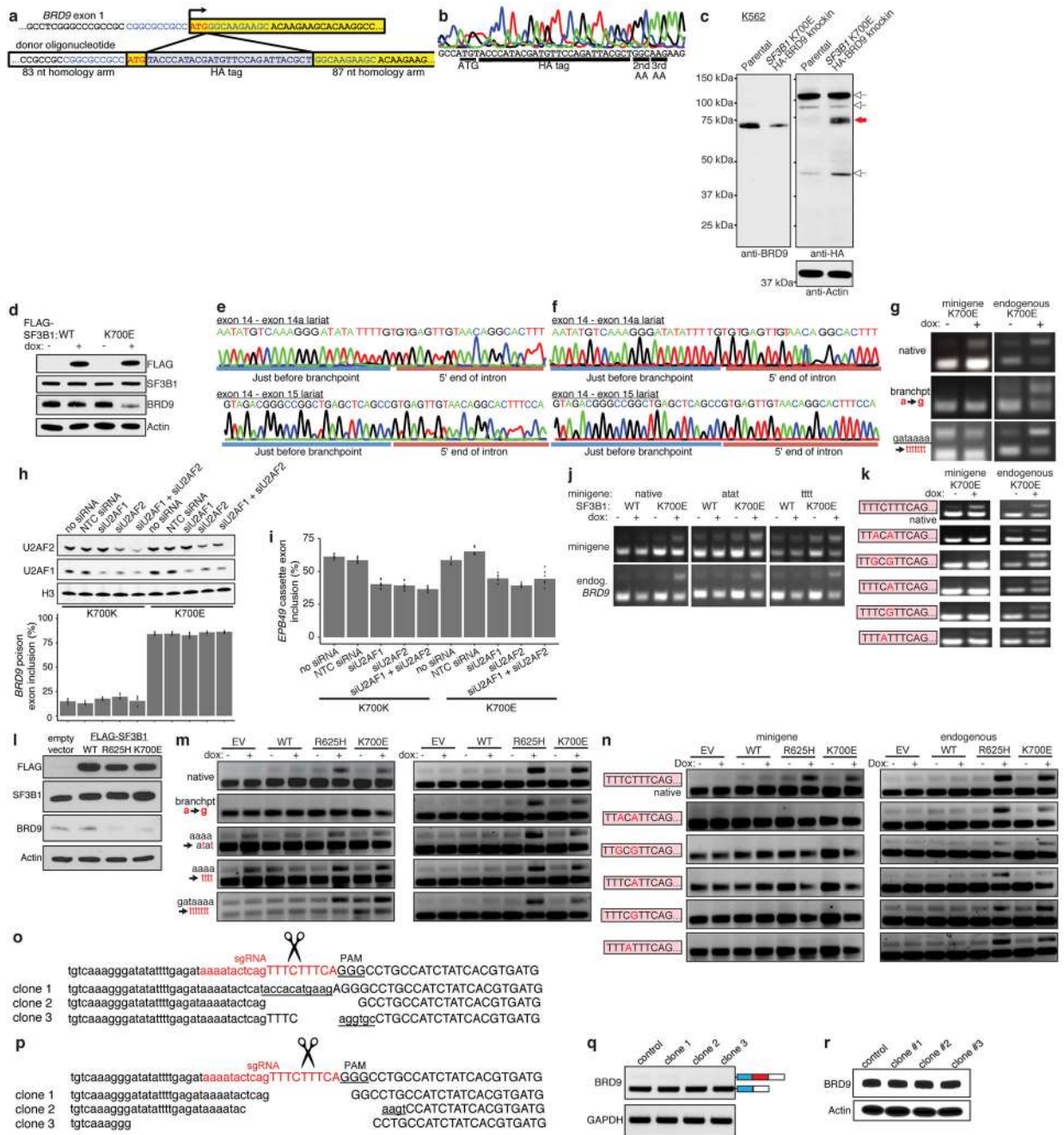
Extended Data Figure 2. Mutant SF3B1 recognizes an aberrant branchpoint within *BRD9* to promote poison exon inclusion, causing loss of full-length BRD9 protein.

(**a**) Schematic illustrating the strategy for knockin of an HA tag into the endogenous *BRD9* locus. The single-stranded donor DNA contained a 197 nt fragment, including 83 nt homologous to the *BRD9* 5' UTR (upstream of the HA tag) and 87 nt homologous to *BRD9* exon 1 (downstream of the start codon).

(**b**) Sanger sequencing of genomic DNA validating successful HA tag knockin in K562 *SF3B1*K700E cells. Representative images from n=2 biologically independent experiments.

(**c**) Western blot with anti-BRD9 (left), anti-HA (right, top), or anti-Actin (right, bottom) used to probe K562 *SF3B1*K700E cells carrying an endogenously N-terminal HA-tagged BRD9. White arrows, non-specific bands. Red arrow, expected size of BRD9 protein. Representative images from n=3 biologically independent experiments.

(**d**) Western blot for FLAG, SF3B1, and endogenous BRD9 protein in MEL270 cells with doxycycline-inducible FLAG-SF3B1-WT/K700E. Representative images from n=3 biologically independent experiments.

(**e**) Sanger sequencing of cDNA arising from reverse transcription of lariats arising from inclusion (top; exon 14 - exon 14a splicing) or exclusion (bottom; exon 14 - exon 15 splicing) of the *BRD9* poison exon in MEL270 cells with doxycycline-inducible FLAG-SF3B1-WT (bottom)/K700E (top). The branchpoints are illustrated in Fig. 2a. Representative images from n=3 biologically independent experiments.

(**f**) As (**e**), but for T47D cells. Representative images from n=3 biologically independent experiments.

(**g**) As Fig. 2b, but for the indicated minigene mutagenesis in T47D cells with doxycycline-inducible FLAG-SF3B1K700E. Representative images from n=3 biologically independent experiments.

(**h**) Western blot of U2AF2, U2AF1, and histone H3 in K562 cells transfected with siRNA against *U2AF1* and/or *U2AF2* (top) and bar plot illustrating mean *BRD9* poison exon inclusion as measured by qPCR following siRNA knockdown of *U2AF1* and/or *U2AF2* (bottom). Experiment performed with n=1 biologically independent replicate for siRNA transfection, n=1 technically independent replicate for Western blot, and n=3 technically independent replicates for RT-PCR. Poison exon inclusion was computed over all n=3x3=9 combinations of technical replicates for RT-PCR for the inclusion and exclusion isoforms. Bars illustrate mean inclusion.

(**i**) *EPB49* cassette exon inclusion as measured by qPCR following siRNA knockdown of *U2AF1* and/or *U2AF2*. As the *EPB49* cassette exon is U2AF-dependent, this experiment serves as a positive control for functional efficacy of *U2AF1* and *U2AF2* KD. n=3 technically independent experiments. Cassette exon inclusion was computed over all n=3x3=9 combinations of technical replicates for RT-PCR for the inclusion and exclusion isoforms. Bars illustrate mean inclusion.

(**j**) As Fig. 2b, but for the indicated minigene mutagenesis in T47D cells with doxycycline-inducible FLAG-SF3B1K700E. Representative images from n=3 biologically independent experiments.

(**k**) As Fig. 2c, but for the indicated minigene mutagenesis in T47D cells with doxycycline-inducible FLAG-SF3B1K700E. Representative images from n=3 biologically independent experiments.

(**l**) Western blot for FLAG, SF3B1, BRD9, and actin in MEL270 cells expressing an empty vector or N-terminal FLAG-tagged SF3B1 wild-type (WT), SF3B1 R625H, or SF3B1 K700E cDNA. Representative images from n=3 biologically independent experiments.

(**m**) RT-PCR analysis of *BRD9* splicing in MEL270 cells expressing doxycycline-inducible empty vector (EV), SF3B1 WT, SF3B1 R625H, or SF3B1 K700E. The left column illustrates minigene splicing while the right column illustrates endogenous *BRD9* splicing. Representative images from n=3 biologically independent experiments.

(**n**) As (**m**), but for the illustrated minigene mutations at the 5' end of the poison exon. Representative images from n=3 biologically independent experiments.

(**o**) Mutations generated at the 5' end of the *BRD9* poison exon by CRISPR/Cas9-mediated insertions and deletions in MEL202 cells (*SF3B1*R625G). The PAM sequence is illustrated with upper-case underlined nucleotides. Red nucleotides hybridize to the sgRNA. Substitutions are illustrated with lower-case underlined nucleotides.

(**p**) As (**o**), but for MEL270 cells. Representative images from n=3 biologically independent experiments.

(**q**) As Fig. 2d (top), but for MEL270 cells. Representative images from n=3 biologically independent experiments.

(**r**) As Fig. 2d (bottom), but for MEL270 cells. Representative images from n=3 biologically independent experiments.
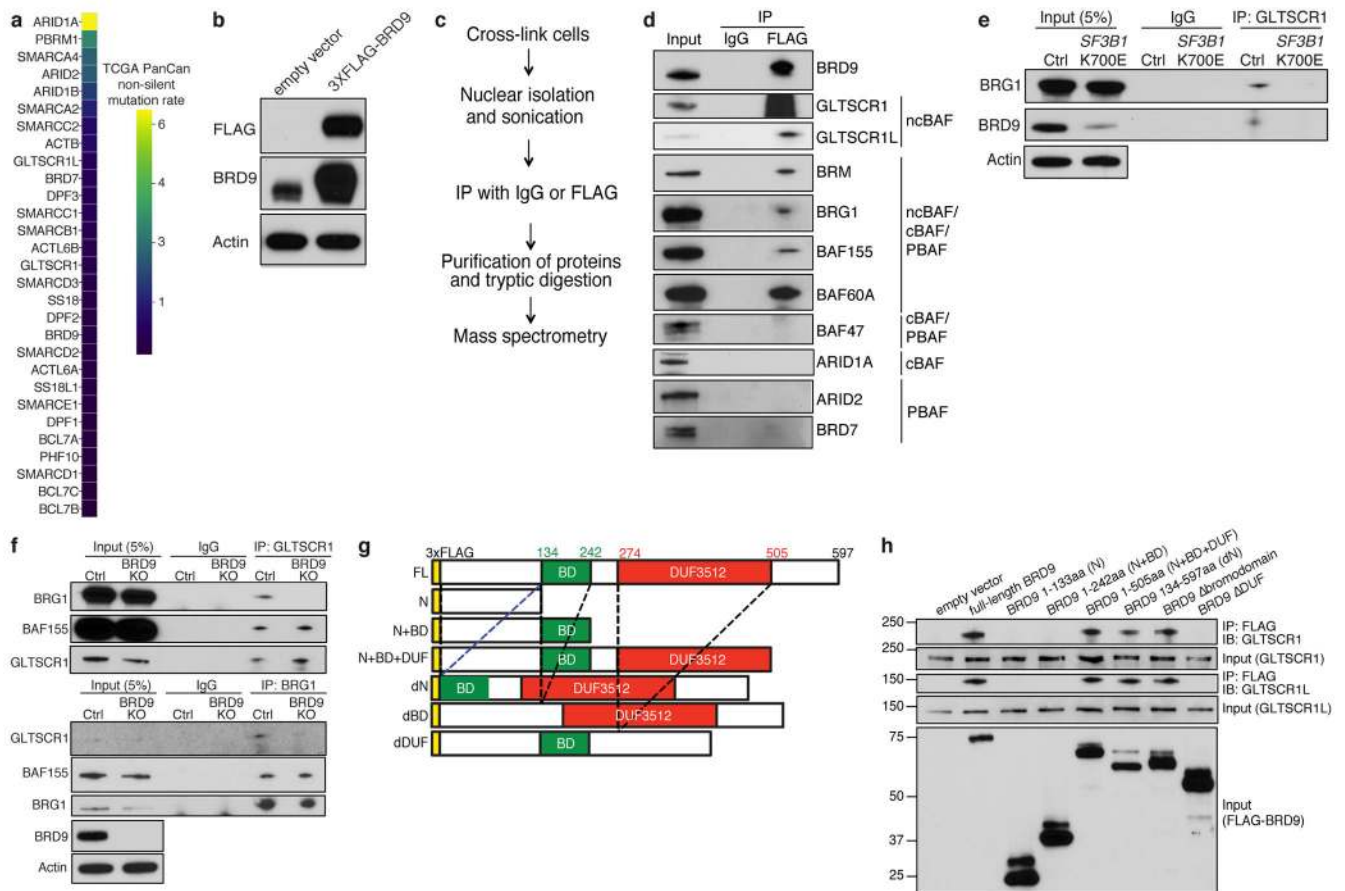
Extended Data Figure 3. BRD9 loss impairs non-canonical BAF complex formation.

(**a**) Mutation rate observed across TCGA cohorts for cBAF, PBAF, and ncBAF components.

(**b**) Western blot confirming FLAG-tagged BRD9 protein expression in 3XFLAG-BRD9-expressing K562 cells. Representative images from n=3 biologically independent experiments.

(**c**) Experimental workflow for using RIME (Rapid Immunoprecipitation Mass spectrometry of Endogenous proteins)[32] for purification and identification of chromatin-associated interactions partners of BRD9.

(**d**) Cross-linking and immunoprecipitation with IgG or FLAG followed by probing with the indicated antibodies. Data from 3xFLAG-BRD9-expressing MEL270 cells. Representative images from n=3 biologically independent experiments.

(**e**) Immunoprecipitation of GLTSCR1 followed by Western blotting with the indicated antibodies in *SF3B1*K700E knockin NALM-6 cells. Representative images from n=3 biologically independent experiments.

(**f**) Immunoprecipitation of GLTSCR1 (top) or BRG1 (bottom) followed by blotting with the indicated antibodies in K562 cells with CRISPR-mediated knockout of BRD9. Representative images from n=3 biologically independent experiments.

(**g**) Schematic of the BRD9 full-length (FL) protein and deletion mutants constructed. BD, bromodomain; DUF, domain of unknown function. "EV": empty vector; "FL": full-length BRD9; "N": 1-133 amino acids (aa) of BRD9; "N+BD": 1-242aa of BRD9; "N+BD+DUF":

1-505aa BRD9; "dN": 134-597aa of BRD9; "dBD": Bromodomain deletion mutant of BRD9; "dDUF": DUF domain deletion mutant of BRD9.

(**h**) Immunoprecipitation (IP) with FLAG following by probing (IB) for GLTSCR1 or GLTSCR1L in 293T cells expressing 3xFLAG-tagged versions of the indicated deletion mutants. Deletion mutants illustrated in (**g**). Representative images from n=3 biologically independent experiments.
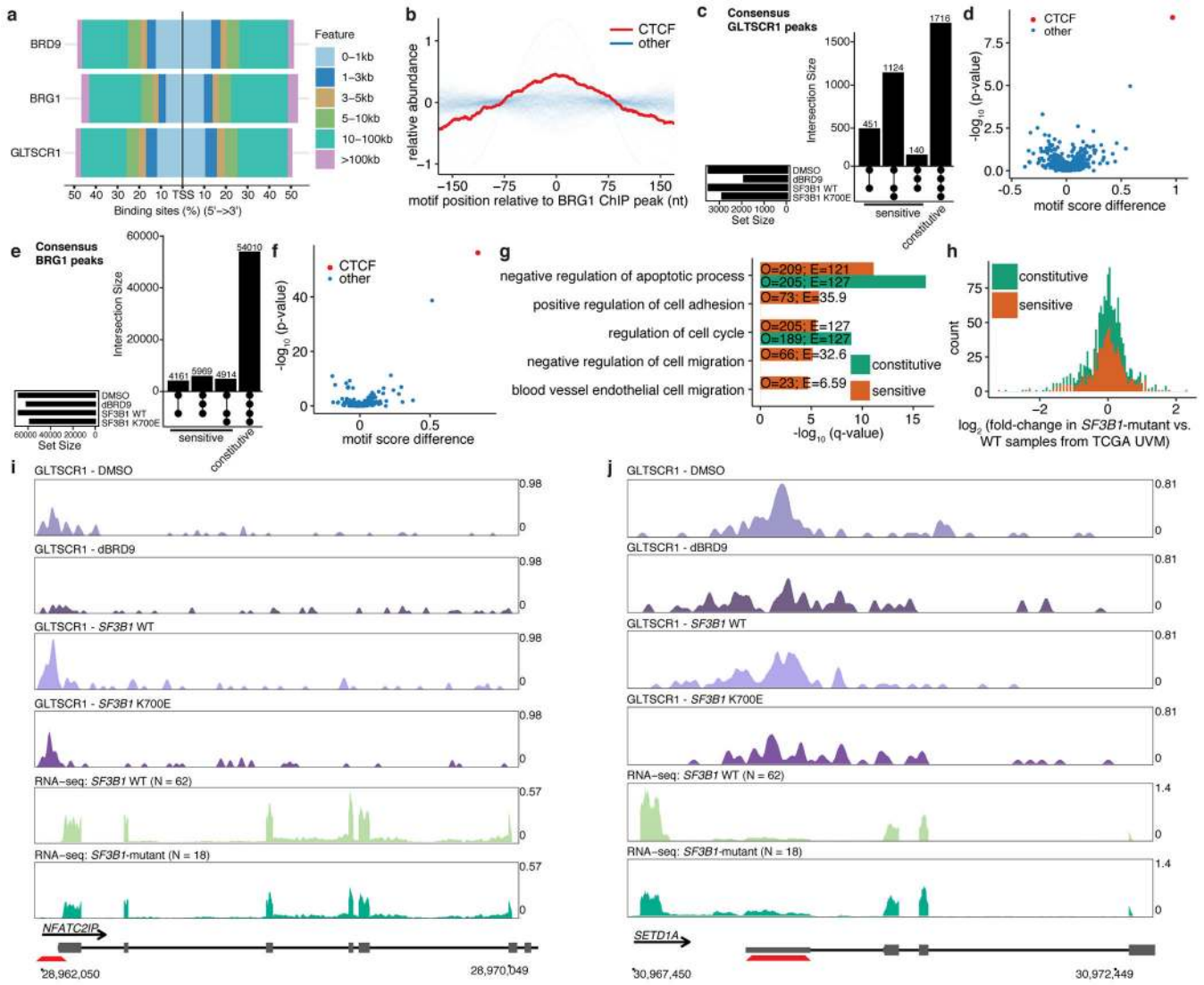
Extended Data Figure 4. BRD9 loss drives relocalization of GLTSCR1 away from CTCF-associated loci.

(**a**) As Fig. 3e, but illustrating relative positions with respect to transcription start sites (TSSs).

(**b**) As Fig. 3f, but for motifs at BRG1-bound loci. n=401 transcription factors analyzed.

(**c**) UpSet plots depicting the overlap of consensus GLTSCR1-bound loci in MEL270 cells with the indicated treatments.

(**d**) Volcano plot illustrating the difference in the mean motif scores at BRD9-sensitive versus constitutive GLTSCR1-bound loci for the transcription factors in Fig. 3f as well as associated statistical significance. n=401 transcription factors analyzed. p-values computed with a two-sided Mann-Whitney U test.

(**e**) As (**c**), but for BRG1-bound loci.

(**f**) As (**d**), but for BRG1-bound loci. n=401 transcription factors analyzed.

(**g**) Selected enriched annotation terms from a GREAT analysis[59] of genes near BRD9-sensitive and constitutive GLTSCR1-bound loci. Plot illustrates $-\log_{10}$ (FDR), computed

with a one-sided binomial test and corrected for multiple testing using the Benjamini-Hochberg procedure. O and E, numbers of genes that were observed and expected.

(**h**) Differences in gene expression in *SF3B1*-mutant versus WT samples in the TCGA UVM cohort for genes with GLTSCR1-bound promoters identified in MEL270 cells. Colors indicate the responsiveness of peaks to BRD9 loss.

(**i**) Read coverage from GLTSCR1 ChIP-seq (MEL270 cells) and RNA-seq (TCGA UVM cohort) around *NFATC2IP*. Red trapezoid indicates GLTSCR1 binding in the promoter, with reduced binding upon treatment with dBRD9 or expression of *SF3B1*K700E. *NFATC2IP* was significantly differentially expressed in UVM samples with *SF3B1* mutations relative to WT samples. Vertical axis scales were rendered comparable by normalizing ChIP-seq read coverage to mapped library size and RNA-seq read coverage to mapped library size, restricted to coding genes. ChIP-seq experiment performed for n=1 biologically independent replicate.

(**j**) As (**i**), but for *SETD1A*. *SETD1A* was significantly differentially expressed in UVM samples with *SF3B1* mutations relative to WT samples.
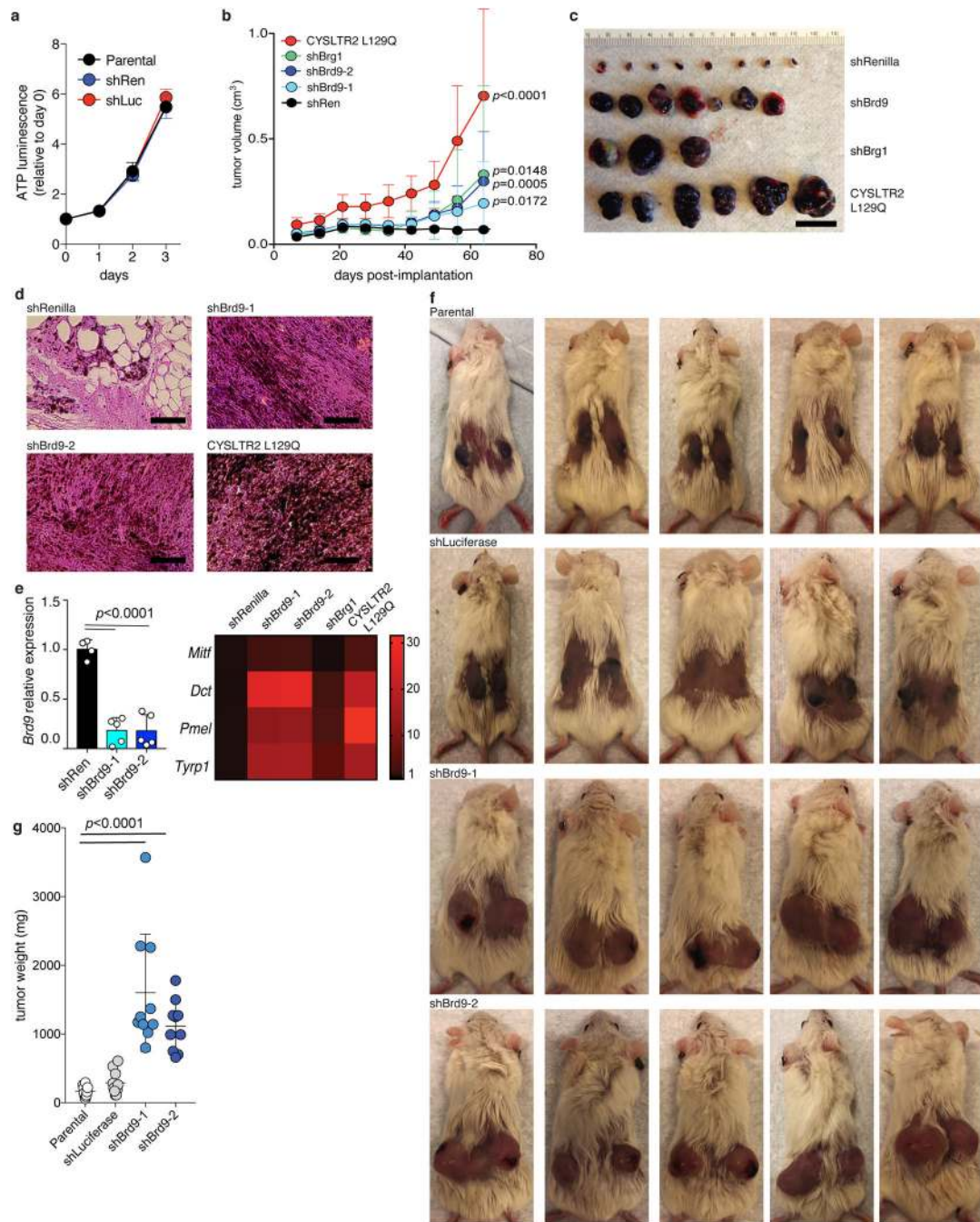
Extended Data Figure 5. BRD9 is a potent tumor suppressor in UVM.

(**a**) *In vitro* growth curves of Melan-a cells treated with two distinct non-targeting shRNAs (shRenilla ("shRen"), shLuciferase ("shLuc")) versus parental, unmanipulated Melan-a cells. n=3 per group. Data are presented as mean ± SD.

(**b**) Tumor volume in SCID mice subcutaneously injected with Melan-a cells expressing a control shRNA (shRen), shRNA against *Brd9* (shBrd9-1 and shBrd9-2), shRNA against *Brg1* (shBrg1), or cDNA encoding CYSLTR2 L129Q (n = 8 mice per group). Data are

presented as mean ± SD. *p*-value at day 64 was calculated compared to shRen group with a two-sided *t*-test.

(**c**) Representative images of the dissected melanomas from (**b**).

(**d**) Hematoxylin and eosin (H&E) images of melanomas from (**b**). Scale bar indicates 100 μm. Representative images from n=3 biologically independent experiments.

(**e**) Quantitative RT-PCR measuring expression of *Brd9* (left) and melanoma-associated genes (*Mitf*, *Dct*, *Pmel*, and *Tyrp1*) of melanomas from (**a**). n=4 (shRen) and n=5 (shBrd9-1 and shBrd9-2) biologically independent experiments. Data are presented as mean ± SD. *p*-value was calculated by two-sided t-test.

(**f**) Images of mice transplanted with parental, unmanipulated Melan-a cells or Melan-a cells transduced with a non-targeting shRNA or Brd9-targeting shRNA. Cells were subcutaneously engrafted into SCID mice and tumor volume was estimated 36 days after transplant.

(**g**) Volumes of tumors from (**f**) at day 36. Data are presented as mean ± SD. n=10 per group. *p*-value was calculated relative to the parental group by a two-sided *t*-test.
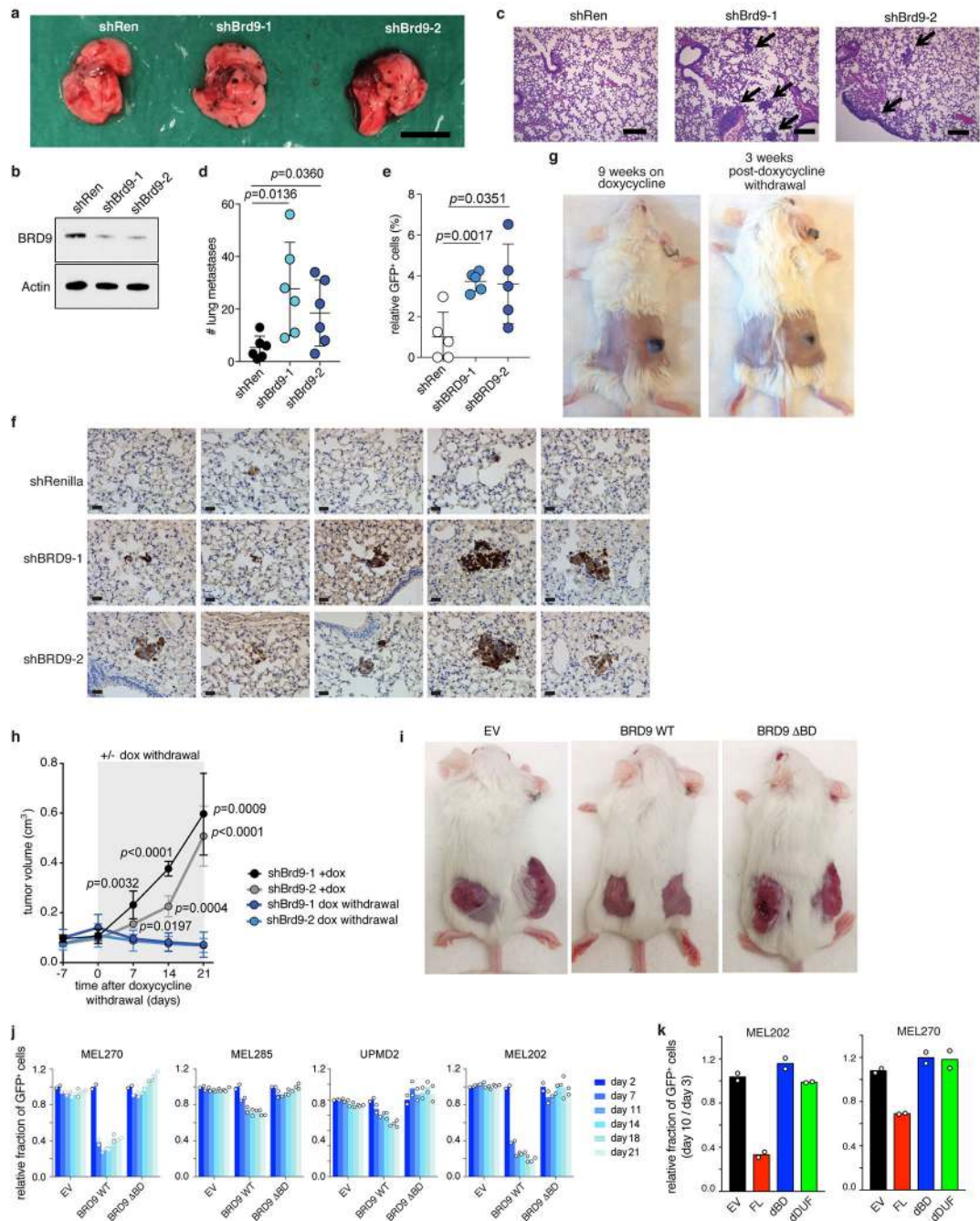
Extended Data Figure 6. BRD9 is a potent tumor suppressor in UVM.
(**a**) Representative images of pulmonary metastatic foci produced 14 days after intravenous injection of B16 cells with or without shBrd9 (MLS-E vector). Scale bar indicates 5 mm.
(**b**) Western blot of endogenous BRD9 in B16 cells immediately prior to injection. Actin, loading control. The experiment was repeated three times with similar results.
(**c**) H&E sections of lung metastases. Arrows indicate metastatic foci. Scale bar indicates 100 μm. The experiment was repeated three times with similar results.

(**d**) Numbers of pulmonary B16 metastases identified in the experiments from (**a**). n=6 per group. *p*-value was calculated relative to the shRen group by a two-sided *t*-test.

(**e**) Relative percentages of GFP$^+$ 92.1 cells with or without shBRD9 (MLS-E vector), assessed by flow cytometric analysis of lung tissue in recipient NSG (NOD-scid IL2R-γ null) mice 14 days following intravenous injection by tail vein. The signal was normalized by dividing by the average percentage of GFP$^+$ cells in the shRen (control) group. n=5 biologically independent experiments per group. *p*-value was calculated relative to the shRen group by a two-sided *t*-test.

(**f**) Anti-GFP immunohistochemistry for sections of lung metastases from the experiment in (**e**). Scale bar indicates 200 μm. The experiment was repeated three times with similar results.

(**g**) Representative images of tumors derived from transplantation of Melan-a cells transduced with dox-inducible shBrd9. Doxycycline was administered for 9 weeks (left) and followed by doxycycline withdrawal for 3 weeks (right).

(**h**) Tumor volume for the experiment in (**g**). n=4 mice per group. The experiment was repeated twice with similar results. *p*-value was calculated relative to the parental group by a two-sided *t*-test at day 7, 14, and 21.

(**i**) Representative images of recipient mice engrafted with MEL270 cells transduced with empty vector (EV), full-length BRD9 (WT), or a bromodomain deletion mutant of BRD9 (BRD9 ΔBD) at day 12. n=5 per group.

(**j**) Results of a competition assay to measure the effects of expression of the indicated cDNAs on growth of the indicated melanoma cells. Transduced cells were identified by co-expression of GFP (pMIGII vector). The percentage of GFP$^+$ cells was tracked over 21 days and normalized to the GFP percentage on day 2. Data are presented as mean ± SD. n=2 per group.

(**k**) Results of a competition assay to measure the effects of expression of the indicated cDNAs on growth of the indicated melanoma cells. Transduced cells were identified by the co-expression of GFP (pMIGII vector). The percentage of GFP$^+$ cells was tracked over 10 days and normalized to the GFP percentage on day 3. n=2 per group.
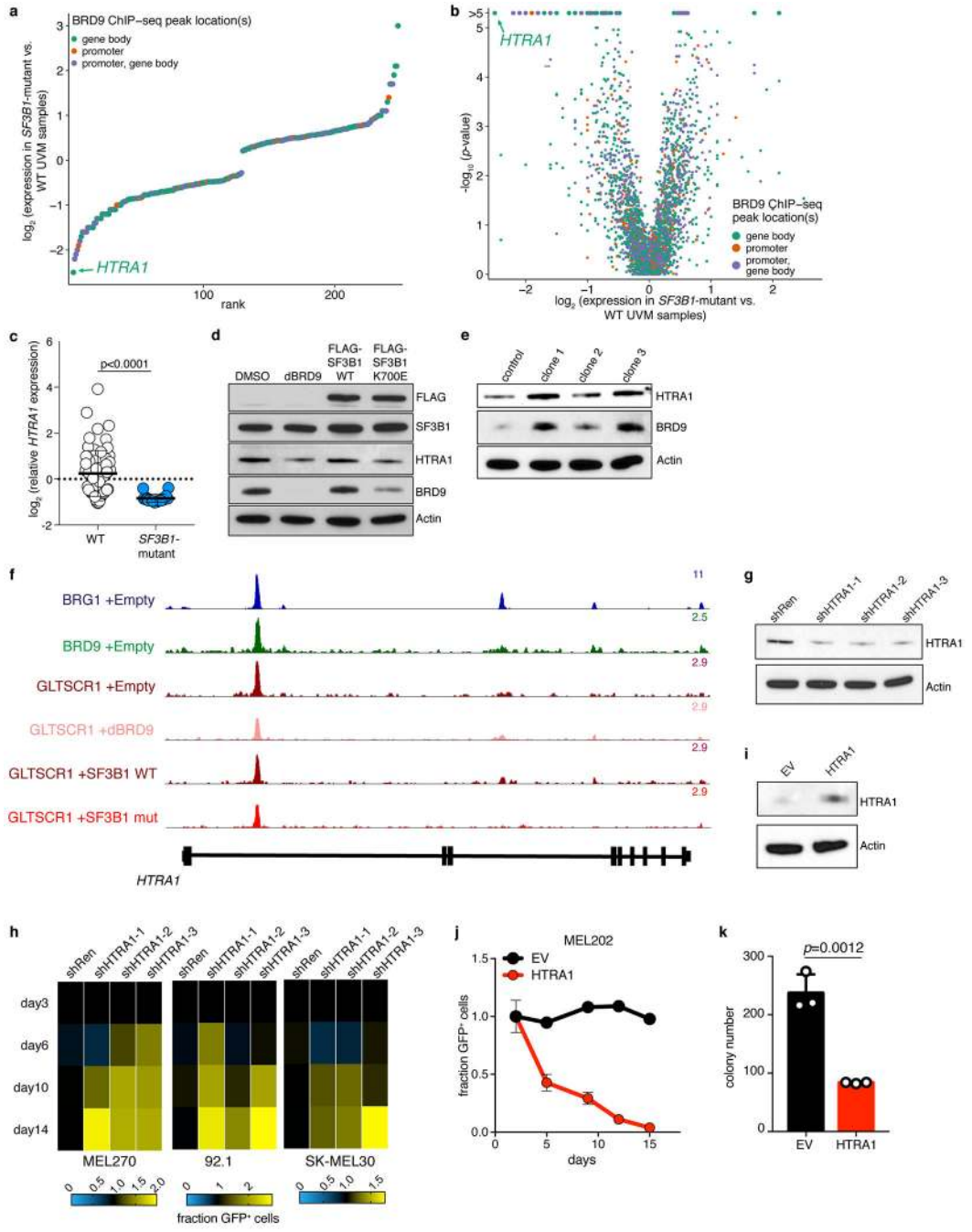
Extended Data Figure 7. BRD9 regulates *HTRA1* expression to promote UVM tumorigenesis.
(**a**) Rank plot illustrating log fold-change of each significantly differentially expressed gene identified by comparing *SF3B1*-mutant to WT patient samples from the TCGA UVM cohort. Plot restricted to genes with BRD9 ChIP-seq peaks within their promoter or gene body in the absence of perturbations to BRD9 (MEL270 cells treated with DMSO or following ectopic expression of WT SF3B1). n=3,122 genes analyzed, of which n=248 met the significance ($p < 0.001$) and expression (median expression in both WT and mutant

samples >2 transcripts per million) thresholds and so were illustrated here. *p*-value computed with a two-sided Mann-Whitney U test.

(**b**) As (**a**), but a volcano plot additionally illustrating the *p*-value associated with the comparison between *SF3B1*-mutant and WT samples. n=3,122 genes analyzed and illustrated. *p*-value computed with two-sided Mann-Whitney U test.

(**c**) *HTRA1* expression in TCGA UVM samples with (n=18) or without (n=62) *SF3B1* mutations. Expression is z-score normalized across all samples. Data are presented as mean ± SD. *p*-value computed with two-sided *t*-test.

(**d**) Western blot for FLAG, SF3B1, HTRA1, BRD9, and actin in *SF3B1*-WT MEL270 cells treated with DMSO, dBRD9, FLAG-SF3B1 WT cDNA, or FLAG-SF3B1 K700E cDNA. Representative images from n=3 biologically independent experiments.

(**e**) Western blot for HTRA1, BRD9, and Actin in MEL202 cells (*SF3B1*R625G) following CRISPR/Cas9-mediated mutagenesis of the *BRD9* poison exon (as shown in Extended Data Fig. 2o). Representative images from n=3 technically independent experiments.

(**f**) Read coverage for BRG1, BRD9, and GLTSCR1 ChIP-seq at the *HTRA1* locus in MEL270 cells (**d**) treated with an empty vector, dBRD9, or SF3B1 WT or K700E cDNAs (n=1 ChIP-seq experiment performed for each condition).

(**g**) Western blot for HTRA1 and Actin in MEL270 cells treated with anti-*HTRA1* shRNAs or a non-targeting control shRNA (shRen). Representative images from n=3 biologically independent experiments.

(**h**) Heat map summarizing the results of a competition assay to measure the effect of each indicated shRNA on the growth of Cas9-expressing *SF3B1*-WT UVM cell lines. Cell growth was computed with respect to cells treated with a non-targeting control shRNA (shRen) and the percentages of GFP$^+$ cells at day 14 was normalized to that at day 2. The illustrated values correspond to the mean computed over n=3 biologically independent experiments.

(**i**) Western blot for HTRA1 and actin in MEL202 cells (*SF3B1*R625G) following stable overexpression of an empty vector (EV) or HTRA1 (both in an MSCV-IRES-GFP vector). Representative images from n=3 biologically independent experiments.

(**j**) Ratio of GFP$^+$ to GFP$^-$ MEL202 cells (*SF3B1*R625G) from a competition experiment in which GFP$^+$ cells from (**i**) were seeded at an initial 1:1 ratio with GFP$^-$ control cells. Data are presented as mean of n=2 biologically independent experiments.

(**k**) Colony number of MEL202 cells expressing EV or HTRA1 cDNA from (**i**) following 10 days of growth in soft agar. Data are presented as mean of n=3 biologically independent experiments.
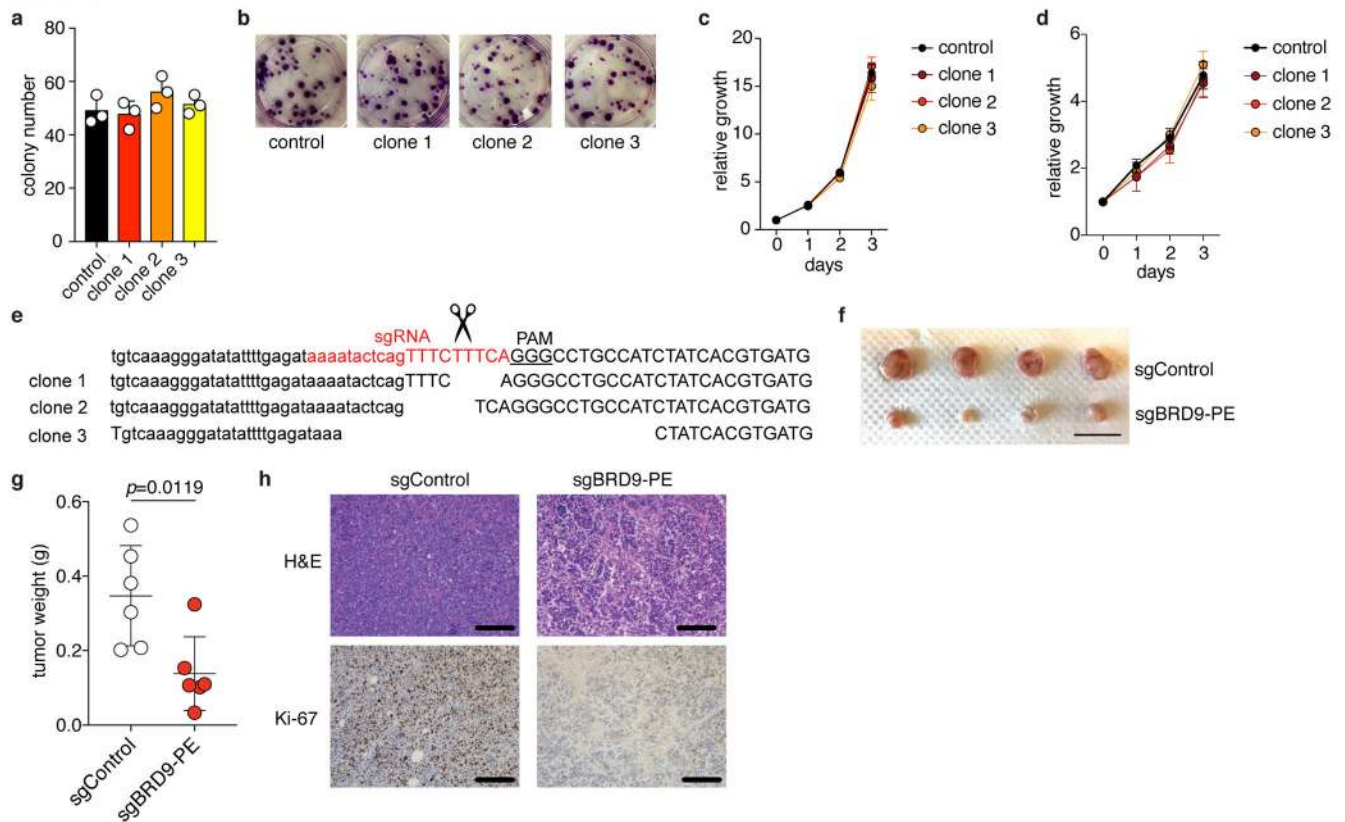
Extended Data Figure 8. CRISPR/Cas9-mediated mutagenesis of the *BRD9* poison exon corrects *BRD9* aberrant splicing and abrogates growth of *SF3B1*-mutant melanoma.

(**a**) Colony number for MEL270 cells (*SF3B1* WT) without (control) or with (clone 1, 2, 3) CRISPR/Cas9-induced indels that disrupted *BRD9* poison exon recognition. Data presented as mean ± SD. n=3 per group.

(**b**) Representative images from (**a**).

(**c**) Proliferation of the clones described in (**a**). n=3 per group.

(**d**) Proliferation of MEL285 cells (*SF3B1* WT) without (control) or with (clone 1, 2, 3) CRISPR/Cas9-induced indels that disrupted *BRD9* poison exon recognition. n=3 per group.

(**e**) Mutations generated at the 5' end of the *BRD9* poison exon by CRISPR/Cas9-mediated insertions and deletions in clones 1-3 of MEL285 cells from (**d**). The PAM sequence is illustrated with upper-case underlined nucleotides. Red nucleotides hybridize to the sgRNA.

(**f**) Representative images of dissected tumors from recipient mice transplanted with CRISPR/Cas9-modified MEL202 clones.

(**g**) Tumor weight for the tumors illustrated in (**f**). Data presented as mean ± SD. n=6 biologically independent experiments per group. *p*-value was calculated relative to the shControl group by a two-sided *t*-test.

(**h**) Hematoxylin & eosin (H&E) as well as Ki-67 immunohistochemistry images for the tumors illustrated in (**f**). Representative images from n=3 independent histological analyses.
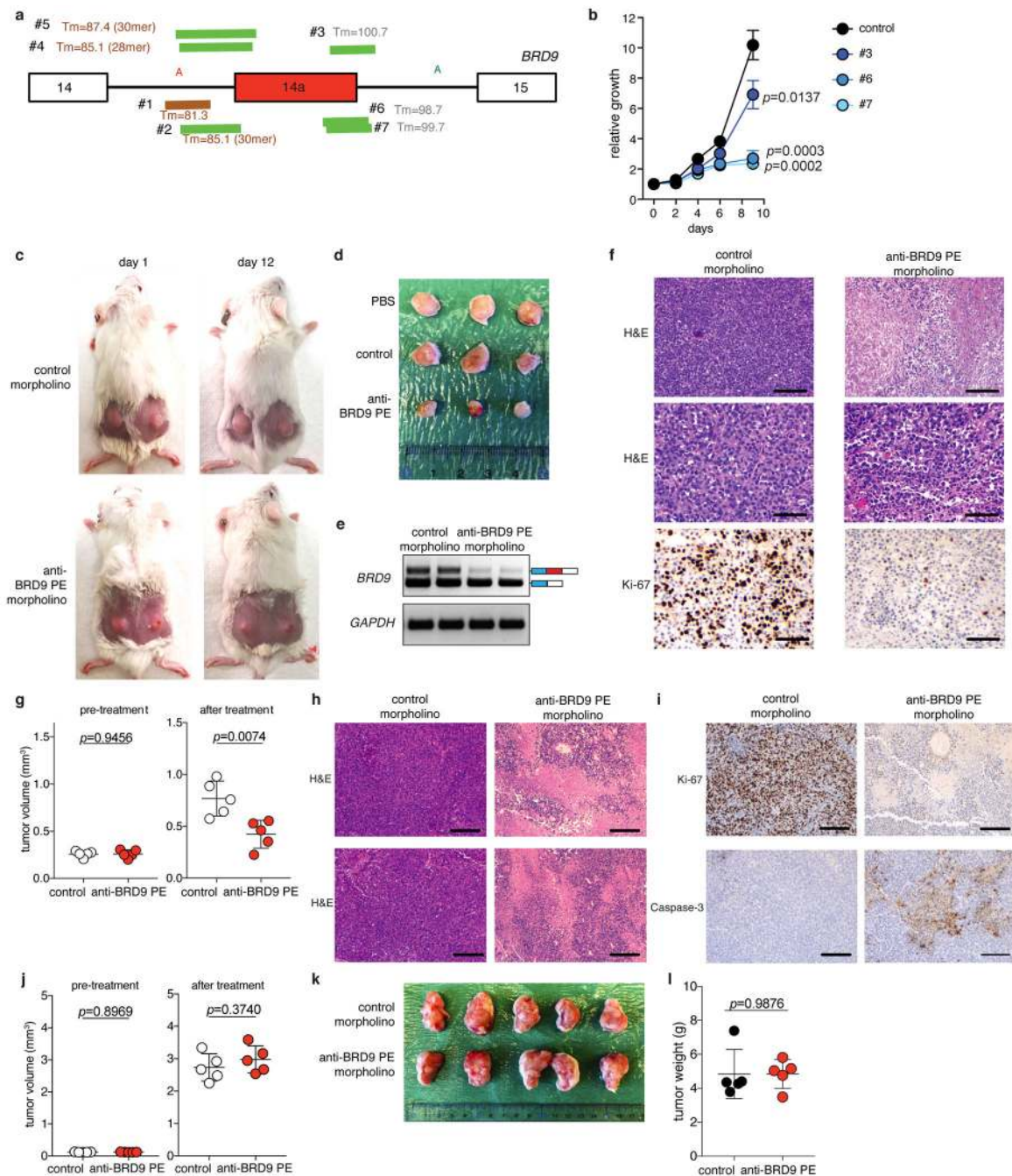
Extended Data Figure 9. Correcting *BRD9* mis-splicing in *SF3B1*-mutant xenografts with antisense oligonucleotides suppresses tumor growth.

(**a**) Cartoon representation of the *BRD9* loci targeted by each designed morpholino. Melting temperature (Tm) is shown. Length of target sequences are indicated in parentheses; if not indicated, then length is 25 nt.

(**b**) Growth of MEL202 cells (*SF3B1*R625G) treated with 10 uM of control non-targeting (control) or *BRD9* poison exon-targeting morpholinos (#3, #6, #7). n=3 biologically

independent experiments per group. *p*-value at day 9 was calculated relative to the control group by a two-sided *t*-test.

(**c**) Representative images of recipient mice xenografted with MEL202 cells and treated with PBS or morpholinos *in vivo*. Each tumor was analyzed after *in vivo* treatment with PBS, control morpholino, or anti-BRD9 PE morpholino (#6; 12.5 mg/kg, every other day, 8 intratumoral injections). n=10 per group.

(**d**) Representative images of dissected tumors from the experiment described in (**c**).

(**e**) RT-PCR results of tumors from (**c**) to evaluate *BRD9* splicing. The experiment was repeated three times with similar results.

(**f**) Representative hematoxylin and eosin (H&E) and Ki-67 staining images of tumors from (**c**). Scale bar indicates 100 μm (top) and 50 μm (middle and bottom). The experiment was repeated three times with similar results.

(**g**) Estimated tumor volume for recipient mice transplanted with a PDX model of *SF3B1*R625C rectal melanoma and treated with *in vivo* morpholinos (control or anti-BRD9 PE morpholino #6; 12.5 mg/kg, every other day, 8 intratumoral injections). n=5 per group. Estimated tumor volumes before and after treatment are shown. Data are presented as mean ± SD. *p*-value was calculated relative to the control group by a two-sided *t*-test.

(**h**) Representative H&E staining images of tumors from (**g**). The experiment was repeated three times with similar results.

(**i**) Representative Ki-67 staining images of tumors from (**g**). The experiment was repeated three times with similar results.

(**j**) Estimated tumor volume for recipient mice transplanted with a PDX model of *SF3B1*-WT UVM and treated with *in vivo* morpholinos (control or anti-BRD9 PE morpholino #6; 12.5 mg/kg, every other day, 8 intratumor injections). n=5 per group. Estimated tumor volumes before and after treatment are shown. Data are presented as mean ± SD. *p*-value was calculated relative to the control group by a two-sided *t*-test.

(**k**) Representative images of dissected tumors from (**j**).

(**l**) Tumor weight for tumors from (**k**). n=5 per group. *p*-value was calculated relative to the control group by a two-sided *t*-test.
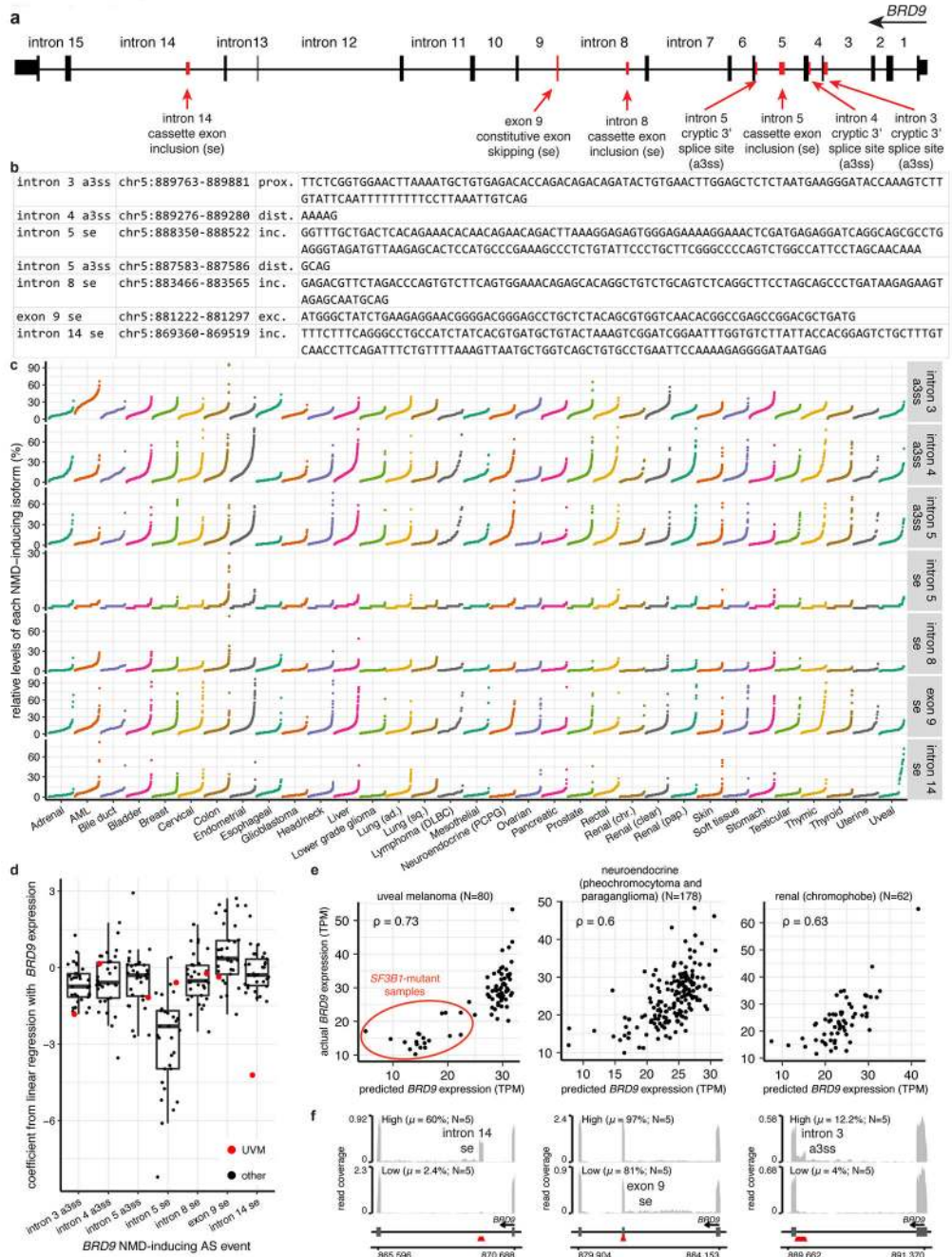
Extended Data Fig. 10. Use of multiple, distinct nonsense-mediated RNA decay (NMD) isoforms of *BRD9*.

(**a**) *BRD9* gene structure illustrating constitutive *BRD9* exons and alternative splicing events that are predicted to induce NMD. *SF3B1* mutations promote inclusion of the BRD9 poison exon in intron 14.

(**b**) Genomic coordinates (hg19/GRCh37 assembly) of each NMD-inducing event illustrated in panel (**a**) as well as genomic sequence of each alternatively spliced region highlighted in red in (**a**). Third column indicates the specific isoform that is a predicted NMD substrate

(prox, intron-proximal competing 3' splice site; dist, intron-distal competing 3' splice site; inc, exon inclusion; exc, exon exclusion).

(**c**) Rank plot illustrating levels of each NMD-inducing isoform relative to total *BRD9* mRNA levels for each sample in each indicated TCGA cohort. Boxes illustrate 1st and 3rd quartiles, with whiskers extending to 1.5X interquartile range.

(**d**) Box plot illustrating the distribution of coefficients estimated by fitting a linear model to predict *BRD9* gene expression based on relative levels of each NMD-inducing isoform. The relative levels of NMD-inducing isoforms illustrated in (**c**), as well as *BRD9* gene expression estimates for each sample, were used to construct an independent linear model with robust regression for each TCGA cohort. The coefficients resulting from this model fitting procedure are illustrated in the box plot, where each dot corresponds to the coefficient associated with the corresponding NMD-inducing event for a single TCGA cohort. Coefficients for the TCGA UVM cohort is highlighted in red. The coefficients are typically negative, as expected for NMD-inducing isoforms, with the exception of constitutive exon 9 skipping, for which the coefficients are generally positive, as expected for an event where NMD is induced when a constitutive exon is excluded. The *SF3B1* mutation-responsive poison exon in intron 14 dominates the fit for UVM, as expected. n=33 TCGA cohorts analyzed and illustrated.

(**e**) Scatter plots comparing actual (y axis) and predicted (x axis) *BRD9* expression levels for three TCGA cohorts. Each dot corresponds to a single sample. ρ, Spearman's correlation between actual and predicted values.

(**f**) RNA-seq read coverage plots for patient samples from the TCGA cohorts illustrated in (**e**) for representative alternative splicing events illustrated in (**a**). Each coverage plot illustrates data averaged over the n=5 patient samples from the vertically matched cohort in (**e**) that exhibit the lowest or highest relative expression of NMD-inducing isoform. μ, mean relative expression of the illustrated NMD-inducing isoform, computed over each group of samples.

Supplementary Material

Refer to Web version on PubMed Central for supplementary material.

Acknowledgements.

REFERENCES

1. Yoshida K, et al. Frequent pathway mutations of splicing machinery in myelodysplasia. Nature 478, 64–69 (2011). [PubMed: 21909114]

2. Papaemmanuil E, et al. Somatic SF3B1 mutation in myelodysplasia with ring sideroblasts. N Engl J Med 365, 1384–1395 (2011). [PubMed: 21995386]

3. Wang L, et al. SF3B1 and other novel cancer genes in chronic lymphocytic leukemia. The New England journal of medicine 365, 2497–2506 (2011). [PubMed: 22150006]

4. Seiler M, et al. Somatic Mutational Landscape of Splicing Factor Genes and Their Functional Consequences across 33 Cancer Types. Cell reports 23, 282–296 e284 (2018). [PubMed: 29617667]

5. Alpsoy A & Dykhuizen EC Glioma tumor suppressor candidate region gene 1 (GLTSCR1) and its paralog GLTSCR1-like form SWI/SNF chromatin remodeling subcomplexes. The Journal of biological chemistry 293, 3892–3903 (2018). [PubMed: 29374058]

6. Michel BC, et al. A non-canonical SWI/SNF complex is a synthetic lethal target in cancers driven by BAF complex perturbation. Nat Cell Biol 20, 1410–1420 (2018). [PubMed: 30397315]

7. Gatchalian J, et al. A non-canonical BRD9-containing BAF chromatin remodeling complex regulates naive pluripotency in mouse embryonic stem cells. Nat Commun 9, 5139 (2018). [PubMed: 30510198]

8. Quesada V, et al. Exome sequencing identifies recurrent mutations of the splicing factor SF3B1 gene in chronic lymphocytic leukemia. Nature genetics 44, 47–52 (2012).

9. Furney SJ, et al. SF3B1 mutations are associated with alternative splicing in uveal melanoma. Cancer discovery 3, 1122–1129 (2013). [PubMed: 23861464]

10. Alsafadi S, et al. Cancer-associated SF3B1 mutations affect alternative splicing by promoting alternative branchpoint usage. Nat Commun 7, 10615 (2016). [PubMed: 26842708]

11. Harbour JW, et al. Recurrent mutations at codon 625 of the splicing factor SF3B1 in uveal melanoma. Nature genetics 45, 133–135 (2013). [PubMed: 23313955]

12. Martin M, et al. Exome sequencing identifies recurrent somatic mutations in EIF1AX and SF3B1 in uveal melanoma with disomy 3. Nature genetics 45, 933–936 (2013). [PubMed: 23793026]

13. Cretu C, et al. Molecular Architecture of SF3b and Structural Consequences of Its Cancer-Related Mutations. Molecular cell 64, 307–319 (2016). [PubMed: 27720643]

14. DeBoever C, et al. Transcriptome sequencing reveals potential mechanism of cryptic 3' splice site selection in SF3B1-mutated cancers. PLoS computational biology 11, e1004105 (2015). [PubMed: 25768983]

15. Darman RB, et al. Cancer-Associated SF3B1 Hotspot Mutations Induce Cryptic 3? Splice Site Selection through Use of a Different Branch Point. Cell reports 13, 1033–1045 (2015). [PubMed: 26565915]

16. Hohmann AF, et al. Sensitivity and engineered resistance of myeloid leukemia cells to BRD9 inhibition. Nat Chem Biol 12, 672–679 (2016). [PubMed: 27376689]

17. Gozani O, Potashkin J & Reed R A potential role for U2AF-SAP 155 interactions in recruiting U2 snRNP to the branch site. Molecular and cellular biology 18, 4752–4760 (1998). [PubMed: 9671485]

18. Pineda JMB & Bradley RK Most human introns are recognized via multiple and tissue-specific branchpoints. Genes Dev 32, 577–591 (2018). [PubMed: 29666160]

19. Remillard D, et al. Degradation of the BAF Complex Factor BRD9 by Heterobifunctional Ligands. Angew Chem Int Ed Engl 56, 5738–5743 (2017). [PubMed: 28418626]

20. Martens JA & Winston F Recent advances in understanding chromatin remodeling by Swi/Snf complexes. Curr Opin Genet Dev 13, 136–142 (2003). [PubMed: 12672490]

21. Brien GL, et al. Targeted degradation of BRD9 reverses oncogenic gene expression in synovial sarcoma. eLife 7(2018).

22. Moore AR, et al. Recurrent activating mutations of G-protein-coupled receptor CYSLTR2 in uveal melanoma. Nat Genet 48, 675–680 (2016). [PubMed: 27089179]

23. Baldi A, et al. The HtrA1 serine protease is down-regulated during human melanoma progression and represses growth of metastatic melanoma cells. Oncogene 21, 6684–6688 (2002). [PubMed: 12242667]

24. Chien J, et al. Serine protease HtrA1 associates with microtubules and inhibits cell migration. Molecular and cellular biology 29, 4177–4187 (2009). [PubMed: 19470753]

25. Walker CJ, et al. Genome-wide association study identifies an acute myeloid leukemia susceptibility locus near BICRA. Leukemia 33, 771–775 (2019). [PubMed: 30291333]

26. Stein CA & Castanotto D FDA-Approved Oligonucleotide Therapies in 2017. Mol Ther 25, 1069–1075 (2017). [PubMed: 28366767]

27. Smit A, Hubley R & Green P . RepeatMasker Open-4.0. (http://www.repeatmasker.org, 2013-2015).

28. Cheng DT, et al. Memorial Sloan Kettering-Integrated Mutation Profiling of Actionable Cancer Targets (MSK-IMPACT): A Hybridization Capture-Based Next-Generation Sequencing Clinical Assay for Solid Tumor Molecular Oncology. The Journal of molecular diagnostics : JMD 17, 251–264 (2015). [PubMed: 25801821]

29. Seiler M, et al. H3B-8800, an orally available small-molecule splicing modulator, induces lethality in spliceosome-mutant cancers. Nature medicine (2018).

30. Leeksma AC, et al. Clonal diversity predicts adverse outcome in chronic lymphocytic leukemia. Leukemia (2018).

31. Kim E, et al. SRSF2 Mutations Contribute to Myelodysplasia by Mutant-Specific Effects on Exon Recognition. Cancer cell 27, 617–630 (2015). [PubMed: 25965569]

32. Mohammed H, et al. Endogenous purification reveals GREB1 as a key estrogen receptor regulatory factor. Cell reports 3, 342–349 (2013). [PubMed: 23403292]

33. Fellmann C, et al. An optimized microRNA backbone for effective single-copy RNAi. Cell reports 5, 1704–1713 (2013). [PubMed: 24332856]

34. Robinson MD, McCarthy DJ & Smyth GK edgeR: a Bioconductor package for differential expression analysis of digital gene expression data. Bioinformatics 26, 139–140 (2010). [PubMed: 19910308]

35. McCarthy DJ, Chen Y & Smyth GK Differential expression analysis of multifactor RNA-Seq experiments with respect to biological variation. Nucleic acids research 40, 4288–4297 (2012). [PubMed: 22287627]

36. Wu D & Smyth GK Camera: a competitive gene set test accounting for inter-gene correlation. Nucleic acids research 40, e133 (2012). [PubMed: 22638577]

37. Piva F, Giulietti M, Burini AB & Principato G SpliceAid 2: a database of human splicing factors expression data and RNA target motifs. Hum Mutat 33, 81–85 (2012). [PubMed: 21922594]

38. Katz Y, Wang ET, Airoldi EM & Burge CB Analysis and design of RNA sequencing experiments for identifying isoform regulation. Nature methods 7, 1009–1015 (2010). [PubMed: 21057496]

39. Mashtalir N, et al. Modular Organization and Assembly of SWI/SNF Family Chromatin Remodeling Complexes. Cell 175, 1272–1288 e1220 (2018). [PubMed: 30343899]

40. Dvinge H, et al. Sample processing obscures cancer-specific alterations in leukemic transcriptomes. Proc Natl Acad Sci U S A 111, 16802–16807 (2014). [PubMed: 25385641]

41. Meyer LR, et al. The UCSC Genome Browser database: extensions and updates 2013. Nucleic acids research 41, D64–69 (2013). [PubMed: 23155063]

42. Flicek P, et al. Ensembl 2013. Nucleic acids research 41, D48–55 (2013). [PubMed: 23203987]

43. Li B & Dewey CN RSEM: accurate transcript quantification from RNA-Seq data with or without a reference genome. BMC bioinformatics 12, 323 (2011). [PubMed: 21816040]

44. Langmead B, Trapnell C, Pop M & Salzberg SL Ultrafast and memory-efficient alignment of short DNA sequences to the human genome. Genome biology 10, R25 (2009). [PubMed: 19261174]

45. Trapnell C, Pachter L & Salzberg SL TopHat: discovering splice junctions with RNA-Seq. Bioinformatics 25, 1105–1111 (2009). [PubMed: 19289445]

46. Robinson MD & Oshlack A A scaling normalization method for differential expression analysis of RNA-seq data. Genome biology 11, R25 (2010). [PubMed: 20196867]

47. Wagenmakers EJ, Lodewyckx T, Kuriyal H & Grasman R Bayesian hypothesis testing for psychologists: a tutorial on the Savage-Dickey method. Cognitive psychology 60, 158–189 (2010). [PubMed: 20064637]

48. Kent WJ, et al. The human genome browser at UCSC. Genome research 12, 996–1006 (2002). [PubMed: 12045153]

49. Wickham H ggplot2: Elegant Graphics for Data Analysis., (Springer-Verlag New York, 2016).

50. Zhang Y, et al. Model-based analysis of ChIP-Seq (MACS). Genome biology 9, R137 (2008). [PubMed: 18798982]

51. Consortium EP An integrated encyclopedia of DNA elements in the human genome. Nature 489, 57–74 (2012). [PubMed: 22955616]

52. Huber W, et al. Orchestrating high-throughput genomic analysis with Bioconductor. Nature methods 12, 115–121 (2015). [PubMed: 25633503]

53. Dharmalingam G, C. T soGGi: Visualise ChIP-seq, MNase-seq and motif occurrence as aggregate plots Summarised Over Grouped Genomic Intervals R package version 1.14.0. (2018).

54. Yu G, Wang LG & He QY ChIPseeker: an R/Bioconductor package for ChIP peak annotation, comparison and visualization. Bioinformatics 31, 2382–2383 (2015). [PubMed: 25765347]

55. Tan G & Lenhard B TFBSTools: an R/bioconductor package for transcription factor binding site analysis. Bioinformatics 32, 1555–1556 (2016). [PubMed: 26794315]

56. Kulakovskiy IV, et al. HOCOMOCO: towards a complete collection of transcription factor binding models for human and mouse via large-scale ChIP-Seq analysis. Nucleic acids research 46, D252–D259 (2018). [PubMed: 29140464]

57. Robertson AG, et al. Integrative Analysis Identifies Four Molecular and Clinical Subsets in Uveal Melanoma. Cancer cell 32, 204–220 e215 (2017). [PubMed: 28810145]

58. Pellagatti A, et al. Impact of spliceosome mutations on RNA splicing in myelodysplasia: dysregulated genes/pathways and clinical associations. Blood 132, 1225–1240 (2018). [PubMed: 29930011]

59. McLean CY, et al. GREAT improves functional interpretation of cis-regulatory regions. Nature biotechnology 28, 495–501 (2010).

60. Pollard KS, Hubisz MJ, Rosenbloom KR & Siepel A Detection of nonneutral substitution rates on mammalian phylogenies. Genome research 20, 110–121 (2010). [PubMed: 19858363]
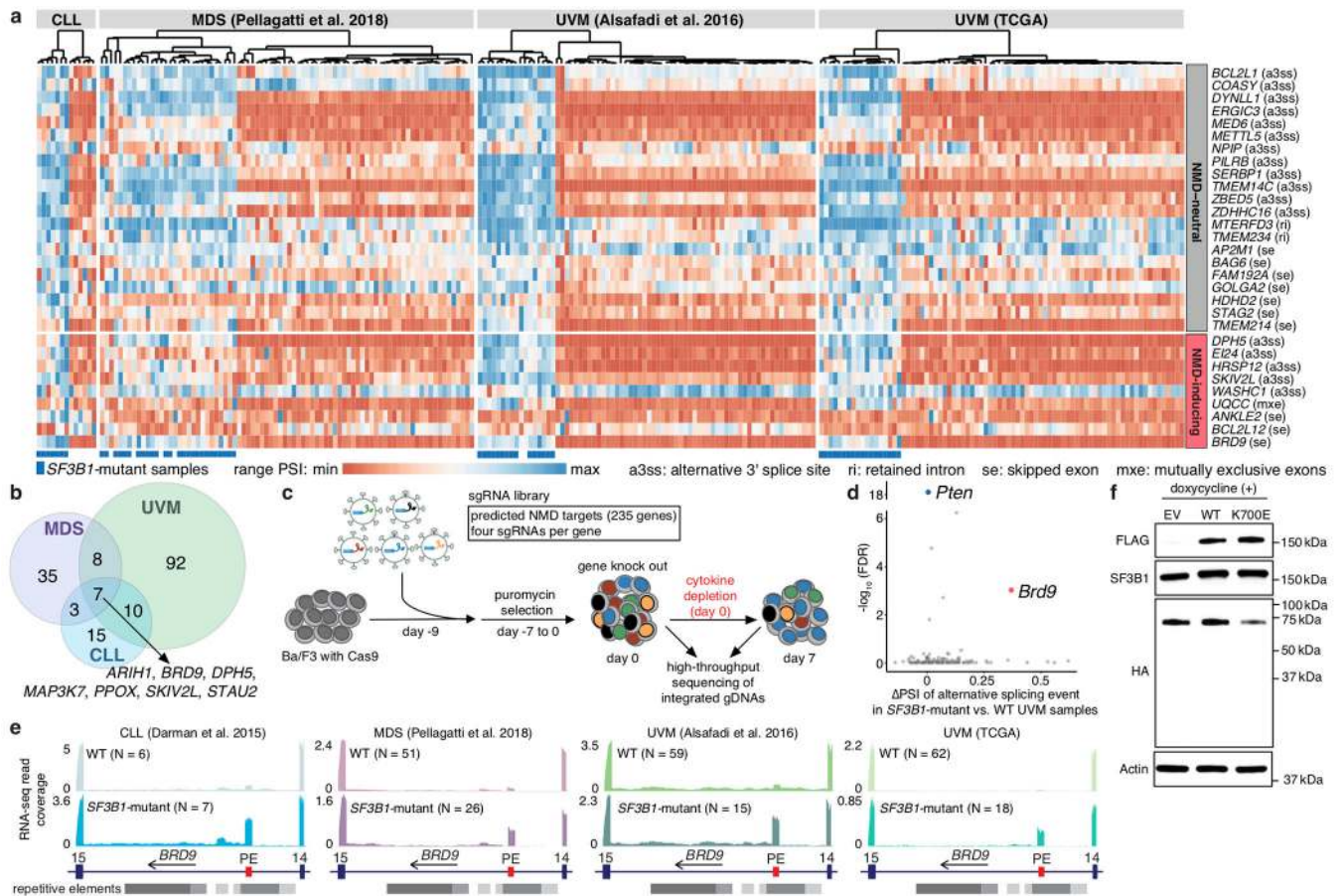
Figure 1. *BRD9* mis-splicing causes BRD9 loss and proliferative advantage in *SF3B1*-mutant cancers.

(**a**) Unsupervised clustering of patient samples based on events differentially spliced in UVM (MEL270) and myeloid leukemia (K562) cells expressing *SF3B1*K700E versus WT. PSI, percent spliced in (fraction of mRNA corresponding to mutant SF3B1-promoted isoform), with per-event, per-cohort range normalization. TCGA, The Cancer Genome Atlas.

(**b**) Genes for which mutant SF3B1 promotes an NMD isoform (a3ss and se events only) in one or more cohorts.

(**c**) CRISPR/Cas9-based positive selection screen targeting genes for which mutant SF3B1 promotes an NMD isoform.

(**d**) Per-gene scatter plot comparing CRISPR screen enrichment (y axis) to differential splicing in TCGA UVM cohort (x axis). *Pten*, positive control. n=6 biologically independent experiments. Per-gene significance computed with two-sided CAMERA test. FDR computed with Benjamini-Hochberg method.

(**e**) *BRD9* RNA-seq read coverage in patient samples. N, number of patients. PE, *BRD9* poison exon; 14 and 15, flanking constitutive exons. Repetitive elements from RepeatMasker[27].

(**f**) Western blot for N-terminal HA-tagged endogenous BRD9 in MEL270 cells transduced with empty vector (EV) or doxycycline-inducible FLAG-SF3B1-WT/K700E. Representative images from n=3 biologically independent experiments.
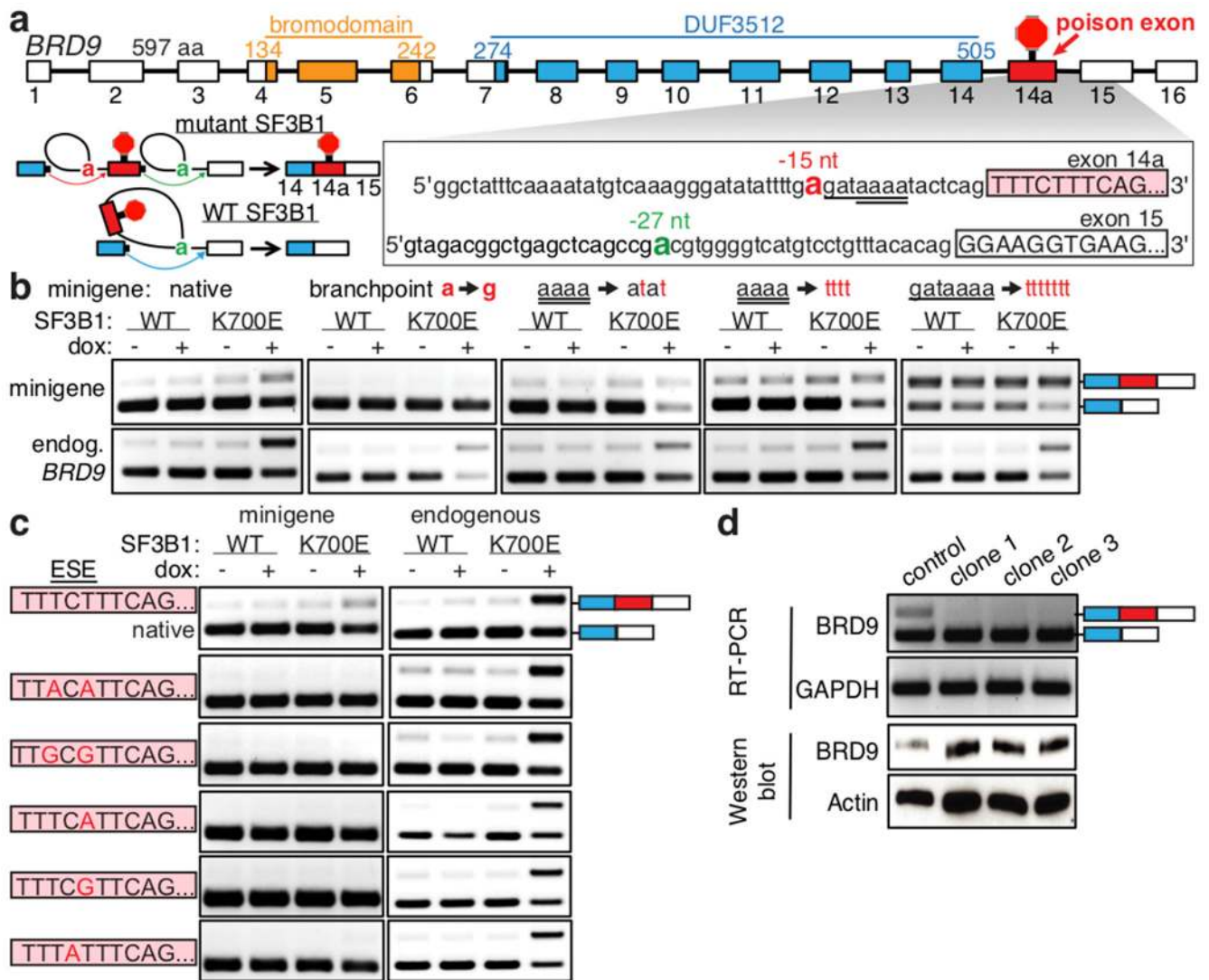
Figure 2. Mutant SF3B1 recognizes an aberrant deep intronic branchpoint within *BRD9*.
(**a**) *BRD9* gene structure and protein domains. Inset illustrates branchpoints used when poison exon is included (top) or excluded (bottom).

(**b**) RT-PCR analysis of *BRD9* poison exon inclusion in a minigene (top) or endogenous (bottom) context following transfection of minigenes with the illustrated mutations into MEL270 cells with doxycycline (dox)-inducible FLAG-SF3B1-WT/K700E. Representative images from n=3 biologically independent experiments. Native, no mutations.

(**c**) As (**b**), but for minigene mutations at the 5' end of the poison exon.

(**d**) RT-PCR (top) illustrating loss of *BRD9* poison exon inclusion and corresponding Western blot (bottom) in MEL202 (*SF3B1*R625G) clones following CRISPR/Cas9-targeting of the poison exon. Indels illustrated in Extended Data Fig. 2o. control, unedited cells. Representative images from n=2 (RT-PCR) and n=3 (Western blot) biologically independent experiments.
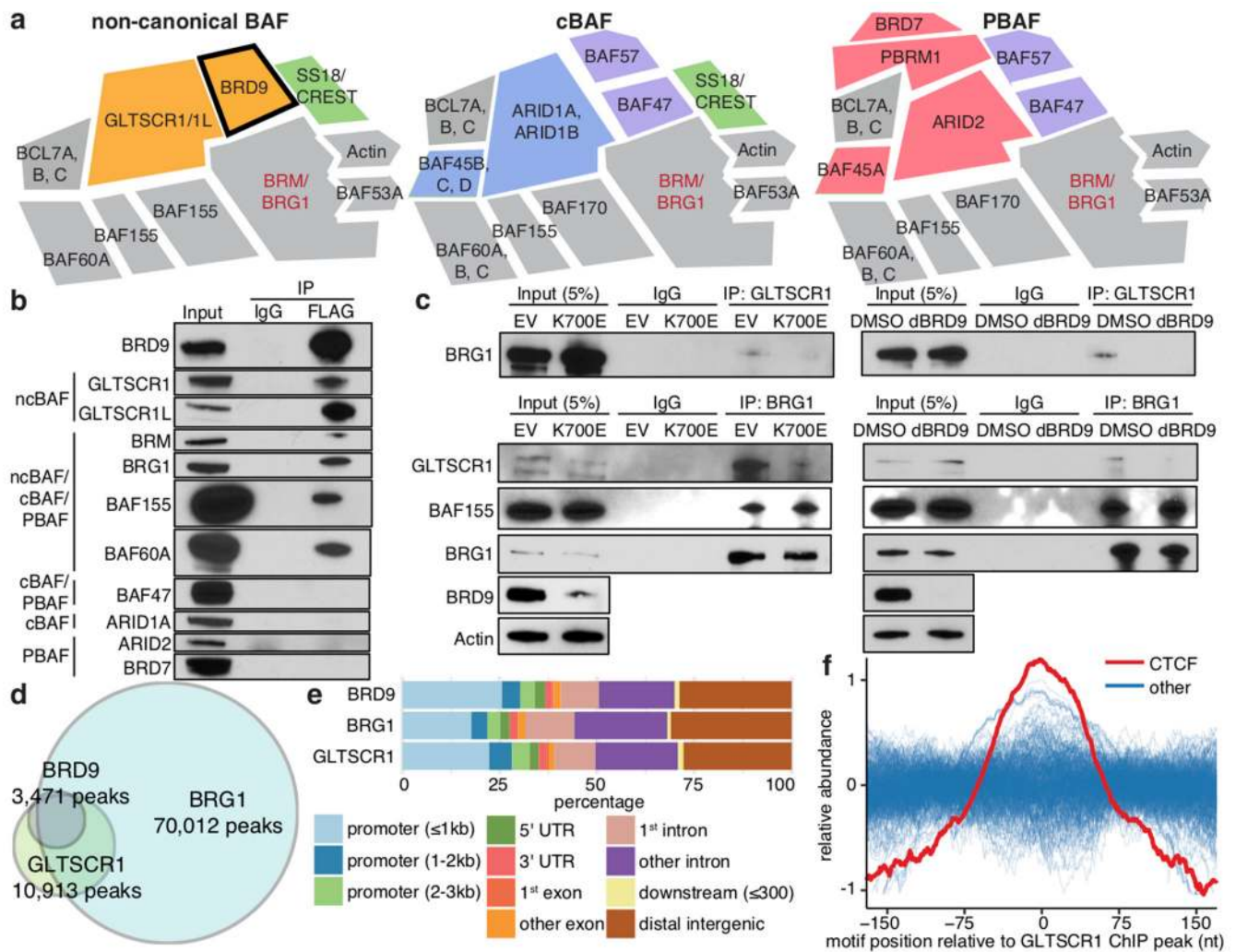
Figure 3. BRD9 loss perturbs non-canonical BAF (ncBAF) complex formation and localization.
(**a**) Schematic of ncBAF, canonical BAF (cBAF), and polybromo-associated BAF (PBAF) complexes[5,6].

(**b**) Cross-linking and immunoprecipitation (IP) with IgG or FLAG followed by immunoblotting in 3xFLAG-BRD9-expressing K562 cells. Representative images from n=3 biologically independent experiments.

(**c**) IP with GLTSCR1 or BRG1 antibody followed by immunoblotting in MEL270 cells expressing exogenous SF3B1 K700E (left) or treated with dBRD9 (BRD9 degrader[19]; right). Representative images from n=3 biologically independent experiments.

(**d**) Overlap of consensus BRD9, BRG1, and GLTSCR1 ChIP-seq peaks called in both MEL270 control samples (DMSO and ectopic SF3B1 WT expression).

(**e**) Genomic localization of BRD9-, BRG1-, and GLTSCR1-bound loci in (**d**).

(**f**) Distributions of transcription factor binding motifs at GLTSCR1-bound loci (20 nt rolling mean). n=401 transcription factors analyzed.
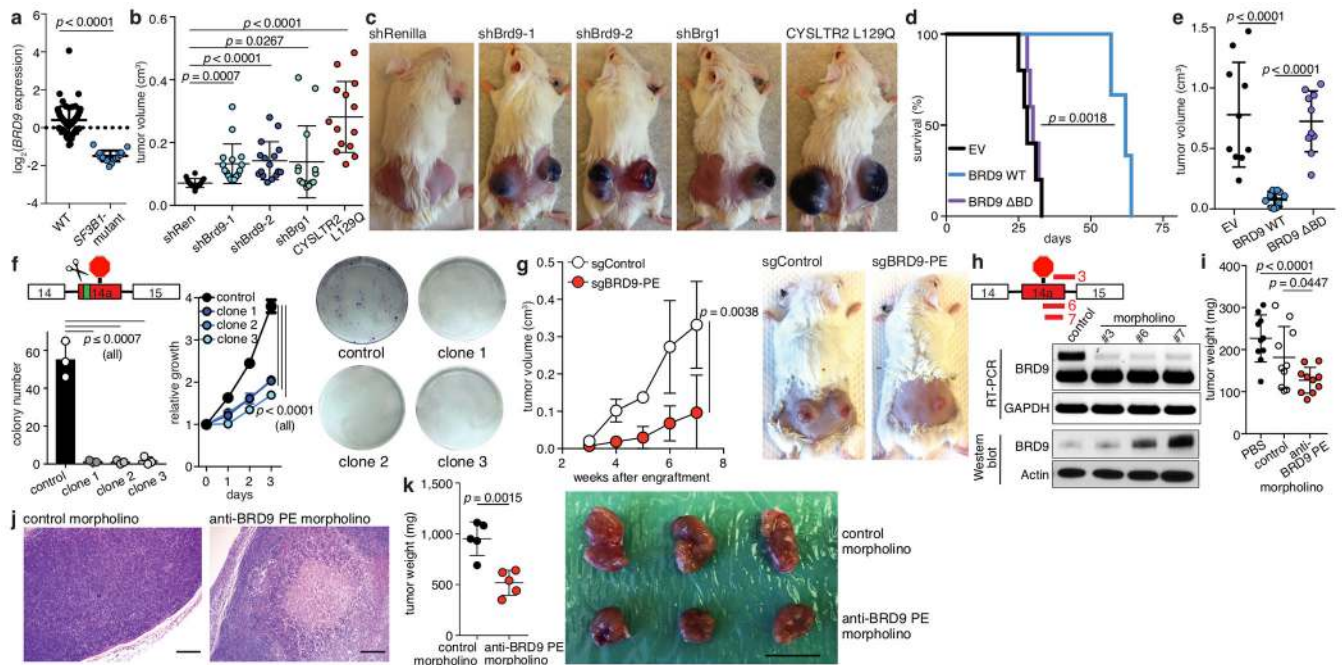
Figure 4. BRD9 is a therapeutically targetable tumor suppressor in melanoma.

(**a**) *BRD9* expression (z-score normalized) in TCGA UVM samples with (n=18) or without (n=62) *SF3B1* mutations. *p*-value calculated by two-sided *t*-test.

(**b**) Tumor volume 49 days after subcutaneous engraftment of Melan-a cells transduced with the indicated shRNAs into SCID mice. n=16, 16, 16, 14, and 14 per group (left to right). Error bars, mean and SD. *p*-value calculated by two-sided *t*-test.

(**c**) Representative mice from (**b**) at day 63.

(**d**) Survival of SCID mice engrafted with MEL270 cells expressing empty vector (EV), full-length BRD9 (WT), or a BRD9 bromodomain deletion mutant (ΔBD) (n=5 per group). *p*-value calculated by log-rank test.

(**e**) Tumor volume from (**d**) 21 days after engraftment. n=10 per group. Error bars, mean and SD. *p*-value calculated by two-sided *t*-test.

(**f**) Colony number (left) and representative images (right) of MEL202 cells (*SF3B1*R625G) without (control) or with (clone 1/2/3) CRISPR/Cas9-induced disruption of the *BRD9* poison exon. Indels illustrated in **Extended Data Fig. 2o.** n=3 biologically independent experiments. Error bars, mean and SD. *p*-value calculated by two-sided *t*-test at day 3 (right).

(**g**) Tumor volume (left) and representative images (right) of mice engrafted with control or clone 1 cells from (**f**). n=6 per group. Error bars, mean and SD. *p*-value calculated by two-sided *t*-test at week 7.

(**h**) ASO design (top), RT-PCR (middle), and Western blot (bottom) for BRD9. MEL202 cells (*SF3B1*R625G) were treated with a non-targeting (control) or targeting morpholino at 10 μM for 24 hours. Representative images from n=3 biologically independent experiments.

(**i**) Tumor weight following 16 days of *in vivo* treatment of MEL202-derived xenografts (*SF3B1*R625G) with PBS or a non-targeting (control) or poison exon-targeting (#6)

morpholino (12.5 mg/kg, every other day, total of 8 intratumoral injections). n=10 per group. Error bars, mean and SD. p-value calculated by two-sided t-test.

(**j**) Hematoxylin and eosin (H&E) images of tumors from (**i**). Scale bar, 200 μm. Representative images from n=3 biologically independent histologic analyses.

(**k**) Tumor weight (left) and representative images (right) following *in vivo* morpholino treatment of a patient-derived rectal melanoma xenograft (*SF3B1*R625C). Scale bar, 1 cm. n=5 per group. p-value calculated by two-sided t-test. Error bars, mean and SD.